

A study on low-noise high-sensitivity multi-aperture camera with selective averaging

メタデータ	言語: en 出版者: Shizuoka University 公開日: 2016-06-15 キーワード (Ja): キーワード (En): 作成者: Bo, Zhang メールアドレス: 所属:
URL	https://doi.org/10.14945/00009589

THESIS

A study on low-noise high-sensitivity multi-
aperture camera with selective averaging

張 博

Department of Nanovision Technology
Graduate School of Science and Technology,
Educational Division, Shizuoka University

December 2015

A Study on Low-Noise High-Sensitivity Multi-Aperture Camera with Selective Averaging

by

Bo Zhang

Submitted for the degree of Doctor of Engineering

February 2016

Abstract

Extremely low-noise and high-sensitivity that enable to distinguish one electron is desired for observation in very dim scenes and for very weak photon emission. In a low-light camera, low-noise high-sensitivity image sensor and fast small F-number lens for collecting more photons, are required to enhance image quality in low-light conditions. For the conventional single lens, with lens F-number decreasing, the lens becomes bulky and costly. To reduce the noise of CMOS image sensors many methods have been presented. The dark current shot noise is suppressed by a pinned photodiode technology. The reset noise and fixed pattern noise are cancelled by the correlated double sampling technique. Column readout noise can be reduced by the high gain column amplifier. The thermal noise and $1/f$ noise can be suppressed by the correlated multiple sampling technique. In recent years, the researches for the low noise CMOS image sensors have focused on the large noise, so-called random telegraph signal (RTS) noise, at in-pixel source follower amplifiers especially in deep submicron technologies. Although RTS noise can be successfully reduced by a buried n-channel in-pixel source follow, the thermal noise is increased due to the reduced transconductance.

The RTS noise becomes one of the dominant noise sources in deep-sub-micro CMOS image sensor technology. It causes bright spots in a low-light

image, which degrades the low-light image quality. To enhance the low-light image quality, in this thesis, low-light image enhancement using a multi-aperture imaging system with a selective averaging method is studied. The multi-aperture imaging system is designed with an array of both lens and CMOS image sensor to increase signal power. One lens and one sensor constitute an aperture like a traditional single-aperture camera. In the multi-aperture imaging system, multiple images can be acquired simultaneously. However, the images are noisy in low-light condition due to poor signal to noise ratio. The noise levels of the corresponding pixels for a subjective point are different each other due to the random noise in each pixel. Although, noise can be reduced by averaging the noisy images, the bright spots which are caused by large sensor noise components such as the RTS noise and large dark current shot noise, cannot be removed. To make matters worse, the number of bright spots in a reproduced image increases due to averaging, which greatly degrade the image quality. The selective averaging is proposed to eliminate the RTS noise and large dark current shot noise. In this method, the variance of every pixel value in dark is measured as pre-processing. In aperture selection, the variances of the corresponding pixels for every reproduced pixel are sorted from minimum to maximum, then only the apertures which can minimize a combination variance, are selected. Different from thresholding, the selected apertures are determined by the minimum combination variance. The RTS noise and large dark current shot noise will cause larger combination variance. Thus, these highly-noise pixels are excluded automatically. Note that the selective averaging is operated pixel by pixel in a reproduced image. In real capturing, the selected apertures are used to calculate the average pixel value of reproduced image.

The effectiveness of selective averaging has been verified by simulation and experiment. In the simulation, the effective noise normalized by the optical gain in the peak of noise histogram is reduced from $1.38e^{-}$ to $0.48e^{-}$ in a 3×3 -aperture system using low-noise CMOS image sensor based on folding-integration and cyclic column ADCs. In the experiment, a prototype 3

$\times 3$ -aperture camera is developed. Under a low-light condition, in which the maximum average signal per aperture is $11e^-$, the RTS noise and dark current white defects are removed and the peak signal-to-noise ratio (PSNR) of the image is increased by 6.3dB. The performance of selective averaging also demonstrated in color using a 2×2 -aperture color camera. The color reproduction errors are quantitatively evaluated by simulation. The root-mean-square in the CIE-xy 1931 color space becomes approximately a half after the selective averaging.

Declaration

The work in this thesis is based on research carried out at the Imaging Devices Laboratory, Research Institute of Electronics, Shizuoka University. No part of this thesis has been submitted elsewhere for any other degree or qualification and it is all my own work unless referenced to the contrary in the text.

Copyright © 2016 by Bo Zhang.

“The copyright of this thesis rests with the author. No quotations from it should be published without the author’s prior written consent and information derived from it should be acknowledged”.

“本論文の著作権は、国立大学法人静岡大学大学院自然科学教育部ナノビジョン工学専攻張博が所有しています。本論文の記事・図面の無断複写、複製および無断転載を禁じます。ただし、著者は本論文の複写権を国立大学法人静岡大学に唯一許諾します”。

List of Figures

1. 1	Noise histogram. (a) EMCCD and (b) high performance CMOS image sensor.	4
1. 2	Structure of a multi-aperture imaging system.	5
2. 1	Block diagram of an electron-multiplying charge coupled device.	13
2. 2	Cross section of single photon avalanche diode.	15
2. 3	Architecture of CMOS image sensor.	16
2. 4	Passive pixel sensor structure.	17
2. 5	Schematic diagram of active pixel sensor. (a) Three-transistor and (b) four-transistor.	18
2. 6	Simplified circuit diagram of a pixel. (a) Schematic and (b) noise model.	24
2. 7	Traps in the silicon band-gap.	26
2. 8	Pixel structure of (a) 4-Tr. APS with pinned photodiode and (b) 3-Tr. APS with surface photodiode.	28
2. 9	Correlated double sampling. (a) Schematic diagram and (b) timing diagram.	29
2. 10	Signal readout chain in CMOS image sensor.	30
2. 11	Relationship between the gain and the noise level or maximum signal level.	31
2. 12	Correlated multiple sampling. (a) Schematic diagram and (b) timing diagram.	32
2. 13	Transfer curve of the folding integration ADC (M=16).	33
2. 14	Cross section of a buried channel n-MOS transistor.	34

2. 15	Structure of a high conversion gain pixel.	36
3. 1	Comparison of (a) multi-aperture imaging system and (b) single aperture counterpart.	46
3. 2	SNRs for different values of amplifier noise. (a) $1.0e^-$ and $0.5e^-$. (b) $0.3e^-$ and $0.1e^-$. (AP: aperture, CP: counterpart)	49
3. 3	Variance calculations in multi-aperture camera.	51
3. 4	Procedure of aperture selection for one pixel.	52
3.5	Noise distributions for different methods. (a) Histogram and (b) cumulative probability.	55
3. 6	Dark image for different methods. (a) Selective averaging, (b) simple averaging, (c) minimum selection, (d) median selection, (e) raw, and (f) single aperture counterpart.	56
4. 1	Multi-aperture camera.	65
4. 2	Chip micrograph.	65
4. 3	Image resizing. (a) Different focal lengths and (b) resizing.	68
4. 4	Flow chart of single image reproduction.	69
4. 5	Reproduced images and reference image. (a) Selective averaging, (b) simple averaging, (c) minimum selection, (d) median selection, (e) raw, and (f) reference.	71
4. 6	Comparison of (a) raw and virtually defocused image, (b) selective averaging, and (c) median selection.	72
5. 1	Photograph of 2×2 multi-aperture color camera.	79
5. 2	Image reproduction flow chart.	80
5. 3	Noise distribution.	81
5. 4	Noise simulation model.	82
5. 5	Reproduced images for (a) selective averaging, (b) simple averaging, (c) raw, and (d) original.	83
5. 6	Distributions for selective averaging, simple averaging, and raw in CIE-xy color space: (a) R, G, B, and W colors and (b) G only.	84

A. 1	Camera model of (a) ideal and (b) real.	94
A. 2	Schematic diagram of disparity correction.	94
A. 3	Disparity correction: (a) Captured images, (b) corrected images, and (c) image registration.	96

List of Table

2. 1	Relationship between floating diffusion capacitance and conversion gain.....	35
4. 1	Performance summary of applied CIS.....	66
4. 2	The peak of noise histogram for each method (dark condition)...	68
4. 3	PSNR of the image in each method and raw.	72
4. 4	The numbers and percentages of the selected apertures.	73
5. 1	Color reproduction errors in CIE-xy color space.....	85

Table of Contents

Abstract	iii
Declaration	v
List of Figures	vi
List of Table	ix
Table of Contents	x
1 Introduction	1
1.1 Background	1
1.2 Motivation and Research Objective.....	5
1.3 Organization of Thesis	7
2 Overview of Conventional Low-Noise High-Sensitivity Image	
Sensors.....	11
2.1 Introduction	11
2.2 Low-Noise High-Sensitivity Imagers.....	13
2.2.1 EM-CCD.....	13
2.2.2 SPAD	14
2.2.3 CMOS Active Pixel Sensor.....	16
2.3 Noise in CMOS Image Sensor	20
2.3.1 Random Noise	20
2.3.2 Fixed Pattern Noise	27

2.4	Noise Reduction Techniques	26
2.4.1	Pinned Photodiode.....	28
2.4.2	CDS	29
2.4.3	High-Gain Amplifier	30
2.4.4	CMS & Folding-Integration Technique.....	31
2.4.5	Buried n-Channel in-Pixel SF	34
2.4.6	High Conversion Gain Pixel	35
3	Noise Reduction by Multi-Aperture Imaging System with Selective	
	Averaging.....	43
3.1	Introduction	43
3.2	Multi-Aperture Imaging System	45
3.2.1	Structure of Multi-Aperture System	45
3.2.2	Merits of Multi-Aperture System.....	45
3.2.3	SNR Analysis in Multi-Aperture System	47
3.3	Selective Averaging.....	51
3.4	Simulation Results	54
3.5	Summary.....	58
4	Implementation of 3 × 3-Aperture Monochrome Camera with Selective	
	Averaging.....	63
4.1	Introduction	63
4.2	3 × 3 Multi-Aperture Monochrome Camera.....	65
4.3	Image Reproduction Procedure	67
4.3.1	Standardization	67
4.3.2	Image Procedure	69
4.4	Experiment Results	71
4.5	Conclusion	74

5 Low-Noise Performance Demonstration by 2×2 -Aperture Color

Camera	77
5.1 Introduction	77
5.2 Multi-Aperture Color Camera & Image Procedure	79
5.2.1 2×2 Multi-Aperture Color Camera	79
5.2.2 Image Procedure	79
5.3 Simulation Results	81
5.4 Conclusion	86
6 Conclusion	89
Appendix.....	93
List of publications	I
Acknowledgements	1

Chapter 1

Introduction

1.1 Background

There are many situations in which a camera works in low-light conditions, such as security, broadcasting, night vision, and astronomical observation. Such cameras require a fast or large aperture lens, advanced image processing techniques, and low-noise high-sensitivity image sensor.

The image quality is limited by both the image noise and blurring. To enhance image quality in low-light conditions, exposure time is usually increased to collect more photons, thereby the signal to noise ratio (SNR) can be increased. However, the time resolution is reduced by increasing exposure time, which will result in image blur in moving scenes. Large pixel is helpful for collecting photons, but pixel count is reduced in the same area of sensor, which will cause lower spatial resolution.

To collect more photons without sacrificing time resolution, aperture size should be increased. In low-light conditions, the larger aperture size the better image quality is. The aperture size is expressed by lens F-number. The smaller the F-number, the larger the aperture size for a certain focal length. The minimum F-number is limited by the lens diameter. There are drawbacks for small f-number lenses. For example below $F/1.0$, not only the size and weight of lens will increase, but the lens aberration will also increase, which causes low spatial resolution. Although the lens aberration can be

corrected by more lens elements, the cost will greatly increase.

Low-light image quality can be enhanced by image processing, such as filtering. There are two categories of filtering. One is spatial domain, and the other is temporal domain filtering. In the spatial filtering, neighboring pixels are used to calculate the output pixel value. Although noise can be suppressed, it also causes a serious damage on the edges of image. The image becomes blurry after filtering. Bilateral filter [1] was proposed to denoise while preserving edges, by smoothing both in spatial domain and intensity domain. In low-light conditions, the effectiveness of bilateral filter is degraded by large noise components of the image sensor and photon shot noise. The temporal filtering reduces noise using successive frames. A motion blur in moving objects will appear, because it is difficult to distinguish real motion from noise. Motion compensated temporal filtering can solve this problem by establishing a reference frame to allow temporal filtering on motion objects. However, the performance is greatly degraded in low-light conditions. An adaptive spatio-temporal filtering [2][3] can be used in low-light image enhancement. However, it makes the filtering very complex.

The low-light image quality can also be enhanced by low-noise image sensor. The image sensor is used to realize optical-to-electrical signal conversion, signal amplification, and analog-to-digital signal conversion. Because noise is added in each step, low-noise image sensor is necessary in low-light conditions.

The solid-state image sensor is mainly categorized into two types, charge coupled device (CCD) image sensors and complementary metal oxide semiconductor (CMOS) image sensors. The modern CMOS image sensor has its origin of MOS image sensor, which was invented by Morrison in 1963 [4]. The CCD was firstly invented as a new signal transporting device by Boyle and Smith at Bell Lab. in 1969 [5]. Before 1990's, the performance of CMOS image sensor was extremely poor due to large noise caused by the immature fabrication processes.

Compared to CMOS image sensors, CCDs had the advantage of low-noise,

high sensitivity and insensitivity to CMOS threshold mismatch and drift, which contributes to high image quality in low-light conditions. Since the buried channel and electron multiplying techniques are applied in CCDs, the low-light performance is greatly increased. However, in CCDs, high voltage and several voltage levels are required for a high charge transfer efficiency. Moreover, CCDs are fabricated using a specialized process with optimized photodetectors. It is difficult to integrate CCDs with a standard CMOS process. Therefore, CCDs typically require an extra supporting chip to provide control signals and perform signal processing, which increase the manufacturing cost.

In CMOS image sensors, it is possible to implement system-on-chip, which can significantly improve the sensor performance and lower the cost. However, the applications of CMOS image sensors in low-light conditions faced great challenges in old days due to large sensor noise. To reduce sensor noise in CMOS image sensor, many techniques were proposed. A 4-transistor active pixel with the pinned structure was developed for dark current reduction and for reset noise and fixed pattern noise (FPN) cancelling by the correlated double sampling (CDS) technique [6]. High-gain amplifiers can be used to reduce the noise of readout circuits [7]. The correlated multiple sampling (CMS) [8] technique was proposed to reduce thermal noise and $1/f$ noise of the readout circuits. A high-performance CMOS image sensor [9] in which the input referred noise is reduced to around $1e^-$ in the peak of noise histogram based on CMS, was developed. Unfortunately, there are some large temporal noise in the CMOS image sensor which is difficult to be reduced. That is due to the in-pixel source follower random telegraph signal (RTS) noise and dark current shot noise.

Figure 1. 1 shows the noise histogram of an electron multiplying CCD (EMCCD) and that of a high-performance CMOS image sensor based on CMS and folding integration techniques [9]. The noise distribution of EMCCD (Fig. 1. 1(a)) is similar to a Gaussian distribution. However, the noise distribution of CMOS image sensor has large noise components, which

consist of RTS noise and dark current shot noise.

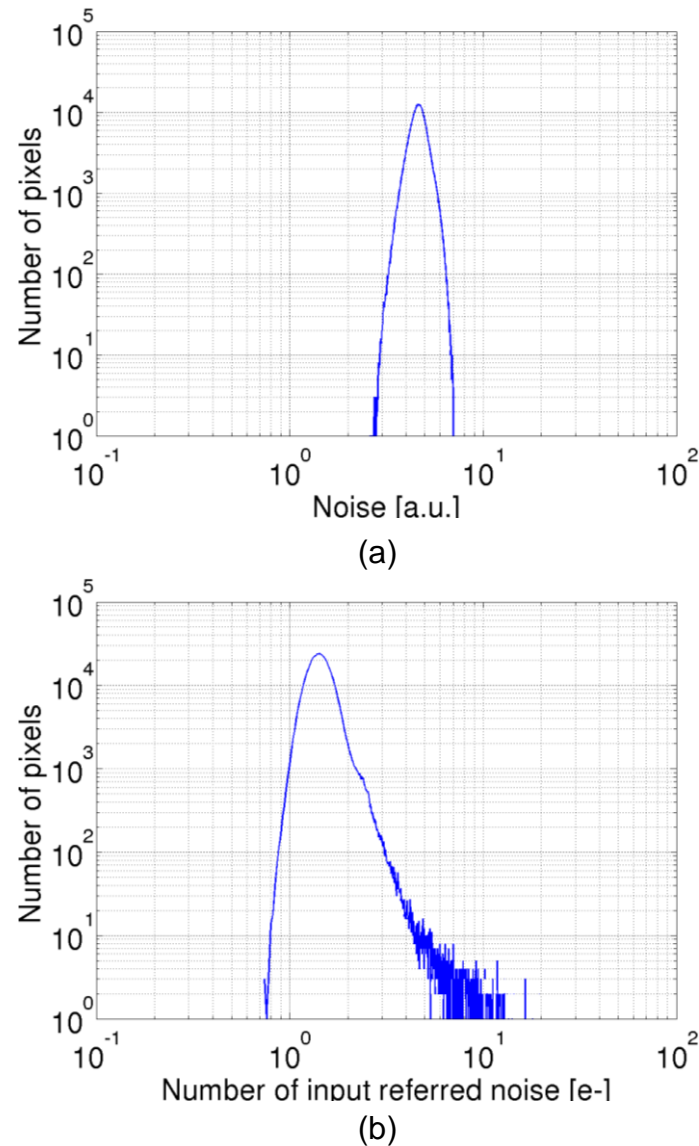


Figure 1. 1 Noise histogram. (a) EMCCD and (b) high performance CMOS image sensor.

RTS noise and dark current shot noise is very visible in low-light conditions due to its large noise level. The low-light image quality is greatly degraded by RTS and large dark current shot noise. RTS noise can be significantly reduced by a buried n-channel source follower [10], but thermal noise is increased due to a reduced transconductance. The dark current has strong temperature dependence. It can be reduced by cooling. However, an extra equipment and power consumption are required in cooling.

1.2 Motivation and Research Objective

In low-light conditions, to increase the number of incident photons, the lens F-number should be as small as possible. With reducing the F-number, not only the lens becomes bulky and costly, but the lens aberrations will increase. Moreover, the minimum F-number is limited by available manufacturing technology (e.g. F/0.4 is unrealistic).

To enhance the low-light imaging performance, in this study, a multi-aperture imaging system with selective averaging is proposed. The structure of multi-aperture imaging system is shown in Figure 1. 2. In this system, both the lens and CMOS image sensor array is utilized. Compared with a single fast lens, lens weight can be greatly reduced. Moreover, a very small synthetic F-number, which is much smaller than F/1.0, can be achieved with the lens array. Multiple images are captured simultaneously in this system. These images are noisy in low-light condition due to very poor SNR. Instead of filtering, the image quality can be enhanced by averaging all the noisy images. Compared with filtering, averaging will not cause any edge blur and motion blurring.

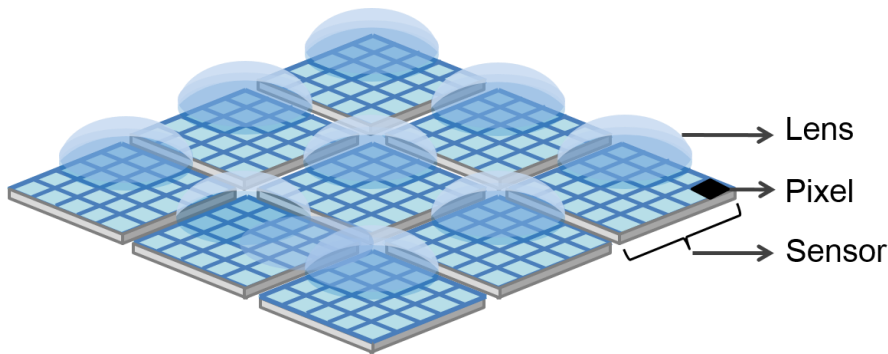


Figure 1. 2 Structure of a multi-aperture imaging system.

As mentioned above, in the CMOS image sensor, there are some large noise components, namely RTS noise and large dark current shot noise. These kinds of noise cause bright noise spot in a low-light image, which will degrade the image quality. Due to the large pixel value, it cannot be removed

by averaging. Moreover, large dark current also causes white noisy defects. To exclude the large noise components specific to the CMOS image sensor before averaging, in this study, a selective averaging method is proposed. In this method, several apertures are selected to minimize the synthetic noise in the dark for each pixel. In real capturing, the pixel value among the selected apertures are averaged to acquire a reproduced image. After selective averaging, the low-light image quality can be improved significantly.

1.3 Organization of Thesis

This thesis consists of six chapters. Chapter 1 introduces research background, motivations, and the organization of this thesis.

In chapter 2, three types of low-noise high-sensitivity imagers such as electron-multiplying (EM) CCD, CMOS single photon avalanche diode (SPAD) image sensor, and CMOS active pixel sensor (APS), are introduced. The advantages and disadvantages of the three imagers are discussed briefly. The noise sources and some of the noise reduction techniques of the CMOS APS are summarized.

Chapter 3 presents a novel noise reduction method by using a multi-aperture imaging system with the selective averaging method. Firstly, the structure and merits of multi-aperture imaging system is introduced. Then, the SNR of the multi-aperture imaging system is analyzed by comparing with the single aperture counterpart. After that, the principle of selective averaging method for large noise removing by excluding the large noise components before averaging is introduced in detail. The simulation shows that the effective noise of the selective averaging in the peak of noise histogram is reduced from $1.38e^-$ to $0.48e^-$ by a 3×3 -aperture system.

In chapter 4, a prototype multi-aperture camera is implemented with a compact 3×3 lens array and a low-noise high-sensitivity CMOS image sensor. Image reproduction procedure of the multi-aperture camera is introduced. The effectiveness of the selective averaging is demonstrated by experiments. In the experiments, peak signal to noise ratio (PSNR) of the reproduced image by selective averaging is increased 6.3dB compared to that of raw image in a low-light condition in which the illumination on the test pattern is 0.04lx. The large noise causing bright spots are completely removed.

Chapter 5 presents the performance of a 2×2 -aperture color camera with the selective averaging. The color reproduction errors are quantitatively

evaluated using CIE-xy 1931 color space. The color reproduction errors of selective averaging in CIE-xy 1931 color space becomes approximately a half when compare with that of the raw.

In chapter 6, a conclusion of this study is presented.

Bibliography

- [1]. C. Tomasi and R. Szeliski, "Bilateral filtering for gray and color images," in Computer Vision, 6th International Conference, pp. 839-846, Jan. 1998.
- [2]. S. W. Lee, V. Maik, J. Jang, J. Shin, and J. Paik, "Noise-adaptive spatio-temporal filter for real-time noise removal in low light level images," IEEE Transactions on Consumer Electronics, vol. 51, no. 2, pp. 648-653, May 2005.
- [3]. H. Malm, M. Oskarsson, E. Warrant, P. Clarberg, J. Hasselgren, and C. Lejdfors, "Adaptive enhancement and noise reduction in very low light level video," in Computer Vision, 11th International Conference, pp. 1-8, Oct. 2007.
- [4]. S. Morrison, "A New Type of Photosensitive Junction Device," Solid-State Electron, vol. 6, no. 5, pp. 485-494, Oct. 1963.
- [5]. W. S. Boyle and G. E. Smith, "Charge-Coupled Semiconductor Devices," Bell System Technical Journal, vol. 49, no. 4, pp. 587-593, Apr. 1970.
- [6]. E. R. Fossum, "Ultra low power imaging systems using CMOS image sensor technology", in Proc. SPIE Advanced Microdevices Space Science Sensors, vol. 2267, pp. 107-111, Sep. 1994.
- [7]. S. Kawahito and N. Kawai, "Noise calculation model for high-gain column amplifiers of CMOS image sensor", in Proc. SPIE, vol. 5017, pp. 48-58, May 2003.

- [8]. N. Kawai and S. Kawahito, "Effectiveness of a correlated multiple sampling differential average for reducing $1/f$ noise", IEICE Electronics Express, vol. 2, no. 13, pp. 379-383, Jul. 2005.
- [9]. M. W. Seo, S. Suh, T. Iida, T. Takasawa, K. Isobe, T. Watanabe, S. Itoh, K. Yasytomi, and S. Kawahito, "A low-noise high intrascene dynamic range CMOS image sensor with a 13 to 19b variable resolution column parallel folding-integration/cyclic ADC," IEEE Journal of Solid-State Circuits, vol. 47, no. 1, pp. 272–283, Jan. 2012.
- [10]. X. Y. Wang, P. R. Rao, and Albert, J. P. Theuwissen, "Characterization of buried channel n-MOST source followers in CMOS image sensor", International Image Sensor Workshop, pp. 223-225, Jun. 2007.

Chapter 2

Overview of Conventional Low-Noise High-Sensitivity Image Sensors

2.1 Introduction

In extremely low-light conditions, image sensor noise that is negligible under ordinary illuminations becomes visible. To enhance the low-light image quality, low-noise high-sensitivity imager is necessary. In this chapter, three types of low-noise high-sensitivity imagers such as EMCCD, SPAD, and CMOS APS, are discussed.

In the EMCCD, an electron-multiplying register is added to the end of the normal serial register to multiply the photo-generated charges by impact ionization. The very high gain in the EMCCD helps to detect a very weak signal, meanwhile, sacrifices the dynamic range. Usually, the EMCCD needs cooling to reduce dark current. In the SPAD, the Geiger mode avalanche diode which is biased above the breakdown voltage is utilized. The SPAD has infinity gain which helps to detect a single photon. However, the SPAD has a dead time, which consists of the quenching and recovery times. In addition, the photon detection probability that carriers generated by a single photon are detected is relatively low. Moreover, the thermally or tunneling

generated carriers which causes dark count exists in SPAD devices.

The CMOS image sensor has advantages of lower cost, low power consumption, and it is easy to achieve system-on-chip. If the noise is reduced to sub-electron level [1][2], the low-noise CMOS image sensor can be used in extremely low-light conditions. The major noise in CMOS image sensors, such as dark current shot noise, thermal noise, reset noise, $1/f$ noise, random telegraph signal (RTS) noise, photon shot noise and fixed pattern noise (FPN), is discussed in this chapter. Dark current consists of diffusion current of minority carriers and generation current in semiconductor under no illumination. Thermal noise due to random motion of electrons in transistors introduces a fluctuation in voltage. Reset noise is also thermal noise which is generated due to the reset transistor and a capacitor, and it causes a fluctuation of voltage in the floating diffusion while the reset transistor is on. $1/f$ noise and RTS noise are caused by the random fluctuation in the number of channel carriers, due to capturing and emission of carriers by traps in the Si-SiO₂ interface. Photon shot noise is the only noise we cannot control. It comes from fluctuation in number of photons shining a pixel, and it causes a fluctuation in the number of electrons. Also, the typical noise reduction methods, which include pinned photodiode, CDS technique, high gain column amplifier, CMS with folding integration technique, buried n-channel source follower, and high conversion gain pixel, are discussed in the following sections.

2.2 Low-Noise High-Sensitivity Imagers

2.2.1 EMCCD

The CCDs (Charge Coupled Devices) have the advantage of low-noise, high-sensitivity [3]-[5]. It is also used in low-light imaging. An advanced CCD, called an electron-multiplying CCD (EMCCD) [6], which was developed to enhance the low-light performance by impact ionization, is specialized in high sensitivity imaging. Figure 2. 1 shows the block diagram of an EMCCD. The EMCCD consists of an image area, a storage area, a horizontal charge transfer CCD (HCCD), and EMCCD, which is similar to a frame-transfer CCD (FTCCD) [7].

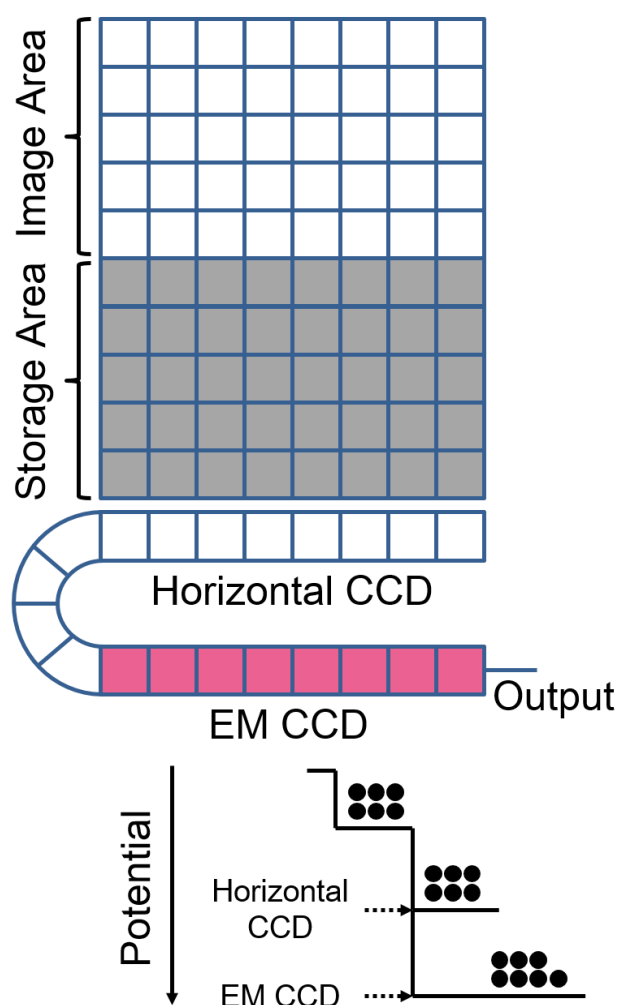


Figure 2. 1 Block diagram of an electron-multiplying charge coupled device.

The storage area, HCCD and EMCCD are covered by a light shield metal. Incident light is absorbed and generates electron-hole pairs in the image area. The generated electrons are gathered and integrated in the potential wells as signal charges. The charges are transferred to the storage area in parallel. After that, the charges are transferred to the HCCD. Unlike the normal FTCCD, in the EMCCD, electron-multiplying register is added to the end of the normal serial register. When charges are transferred through each stage of electron-multiplying register, the secondary electrons are produced by impact ionization. In addition, signal is multiplied before any readout noise addition, which contributes to the low-noise of EMCCD even when operated at a high readout speed.

However, EMCCD has some disadvantages such as requirement of the high voltage and need to be deeply cooled, sacrifice of the dynamic range due to the sensitivity gain and high cost. To multiply electron charges, the EMCCD needs a higher voltage compared the normal CCD. Furthermore, the charge multiplication occurs using impact ionization process, then not only electron charges of the image but also electron charges of thermal noise are amplified. If there is one electron thermally generated, it can be seen as a single pixel noise spike. To suppress the thermal noise electron, the EMCCD requires thermoelectric cooling.

2.2.2 SPAD

The single photon avalanche diode (SPAD) is a semiconductor device based on a p-n junction reverse-biased at a voltage higher than the breakdown. It is also known as a “Geiger mode” avalanche diode. In the Geiger mode, the electric field is so high that a photon generating an electron-hole pair in the depletion region can initiate a self-sustaining avalanche by impact ionization on the lattice. The SPADs have virtually infinity gain, which make it possible in single photon detection.

Figure 2. 2 shows the cross section of a single photon avalanche diode [8]. It has two junctions, the p⁺/n-well junction and n-well/p-substrate junction.

The upper junction provides the multiplication region where the avalanche occurs. To reduce electric potential gradients, a guarding ring which is surrounding the photodiode is designed.

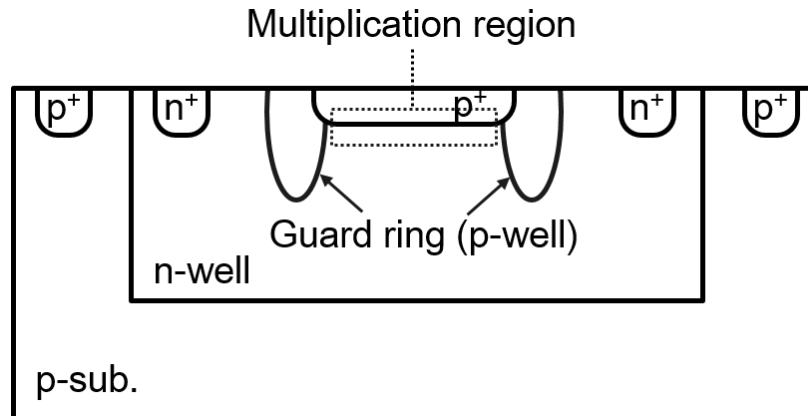


Figure 2. 2 Cross section of single photon avalanche diode.

Owing to low intensity signal detection and high time resolution, the SPAD can be widely used in industrial, biologic and medical applications. For example, Time-Of-Flight (TOF) based 3D imaging [9], molecular imaging, such as fluorescence lifetime imaging microscopy (FLIM) and fluorescence correlation spectroscopy (FCS) [10][11].

In SPADs, quenching and recovery is needed for the avalanche to return to the initial state. The time during quenching and recovery is collectively known as dead time. In addition, not all of photon generated carriers can initiate the avalanche. The photon detection probability (PDP), which is the probability of detected carriers, is relatively low. The PDP is influenced by electric field conditions, doping levels, and the applied voltage. Moreover, noise, such as thermal generated carriers, can also cause undesirable avalanches. In the Geiger mode, it is difficult to distinguish noise causing pulses from regular photon triggered pulses.

2.2.3 CMOS Active Pixel Sensor

In contrast to the CCD, the CMOS image sensor has the advantage of less power requirement, lower cost and it is easy to achieve system-on-chip. However, the CMOS image sensor suffers from poor image quality in a low-

light condition due to a lot of noise sources. On the other hand, the CMOS image sensors have evolved over the years in noise reduction. Now, the CMOS image sensor can be compared favorably with CCD in low-light performance. The details of some noise reduction method will be discussed in Section 2.4.

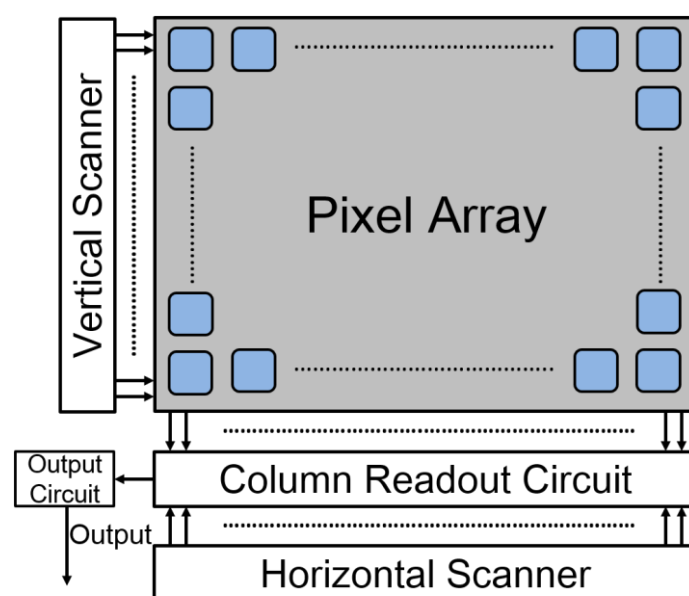


Figure 2. 3 Architecture of CMOS image sensor.

Figure 2. 3 shows the architecture of CMOS image sensor. It consists of a pixel array, column readout circuit, vertical and horizontal scanners, and output circuit. The vertical and horizontal scanners are used to readout all the pixels' output sequentially. A column parallel readout circuit that is known as the noise canceller is included to realize low-noise and high-sensitivity. Pixel is an important part in CMOS image sensor. A lot of novel pixel architectures are designed to enhance the performance, such as low dark current, wide DR, high speed, and so on. The pixel consists of a photodiode and some transistors. The photodiode is used for photon to charge conversion. The transistors can achieve the charge transfer, storage, and amplification.

The early CMOS image sensor actually was based on passive pixel sensor (PPS). Figure 2. 4 shows the structure of PPS, which is comprised of a photodiode and a readout switch. Owing to the simple structure of the PPS,

high resolution can be achieved easily by scaling down the pixel size. However, the image quality is very poor due to very large noise. In contrast of the PPS, the active pixel sensor (APS), which consists of a photodiode and an in-pixel amplifier, was developed.

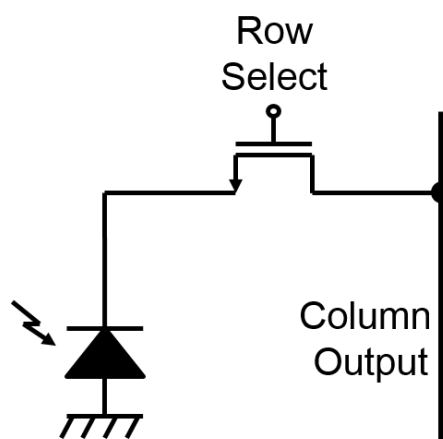


Figure 2. 4 Passive pixel sensor structure.

Figure 2. 5 (a) shows the structure of 3-Tr. APS. It consists of a photodiode and 3 n-MOS transistors: a reset transistor (RST), an in-pixel amplifier transistor, and a row select transistor (SEL). Firstly, the photodiode is reset to VDD through RST. After that, the photo-generated charges are collected. The collected charge is amplified afterwards by the source follower amplifier and read out through the row select transistor. Since only three transistors are used inside the pixel, the fill factor of 3-Tr. pixels is larger than most of the other APS pixels. Moreover, the photodiode can be reversely biased using a high positive potential through RST, which results in a wide depletion region, both the quantum efficiency and full-well capacity for 3-Tr. APS are excellent. However, the 3-Tr. APS is subject to reset noise, which is typically the dominant source of pixel noise. CDS is a method to cancel the reset noise and FPN. In CDS, two samples are taken. One when the pixel is still in the reset state, and the other when the charge has been transferred to the readout node. If the same noise is added to the two values, the noise can be removed by taking the difference of these two values. Because the true CDS operation to remove the reset noise is difficult to implement in 3-Tr. APS, a 4-Tr. APS was developed.

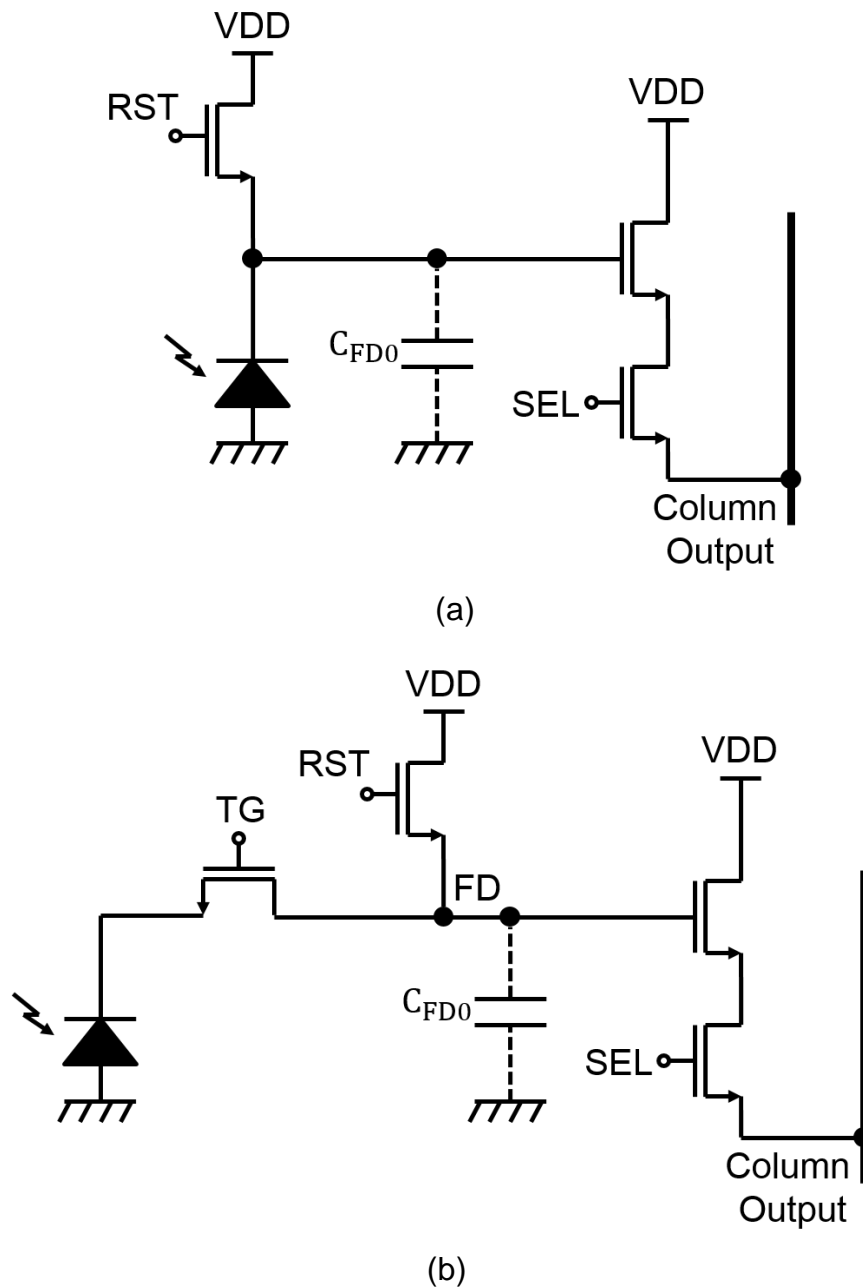


Figure 2. 5 Schematic diagram of active pixel sensor. (a) Three-transistor and (b) four-transistor.

Figure 2. 5 (b) shows the structure of 4-Tr. APS, which consists of a photodiode, a transfer gate (TG), a reset transistor, a source follower amplifier, and a row select transistor. The photo-generated electrons are collected in the photodiode during the exposure time. Then, the FD is reset to remove any residual charges. The reset level of the FD is determined by the reset mode of RST transistor. After that, the TG is switched on to transfer the stored electrons in the photodiode to the FD. Meanwhile the photodiode

is automatically reset and ready for the next integration operation. Transferred electrons drop in the potential well at the FD node, then the source follower amplifier output is decreased. The signal level of the pixel output is sampled after the charge transfer process is completed. The difference between two sampled outputs for the reset level and the signal level of pixel outputs is taken for performing the pixel noise cancelling. Due to its significant improvement on noise reduction, the 4-Tr. APS becomes the most popular design for high-quality image applications.

2.3 Noise in CMOS Image Sensor

Noise in CISs is typically classified into two categories: random noise and fixed pattern noise. In this section, the sources of noise are discussed.

2.3.1 Random Noise

Photon shot noise

Light is composed of photons, which are emitted by a source at random. For this reason, the amount of photons is not constant in time, and exhibits detectable statistical fluctuations. Because of its nature, it does not depend on the quality of detector and is unavoidable.

The random process of light emission can be modeled using the Poisson probability distribution, which is expressed as

$$P_N = \frac{(\bar{N})^N \cdot \exp(-\bar{N})}{N!} \quad 2.1$$

$$\bar{N} = \sum_0^{+\infty} N P_N \quad 2.2$$

where, P_N is the probability, N and \bar{N} are the actual number and mean number of photons, respectively. The variance of photon shot noise is given by

$$\sigma_N^2 = \sum_0^{+\infty} (N - \bar{N})^2 P_N = \overline{N^2} - \bar{N}^2 = \bar{N} \quad 2.3$$

here σ_N is the standard deviation.

In image sensors, the standard deviation is referred to the amount of noise. It equals the square root of the mean number of photons. Although, the noise increases with the number of photon increasing, the SNR of image sensor also increases when the number of photons increases. The larger the number of photon, the better the sensor's SNR.

Dark current shot noise

Another shot noise in CIS is the dark current shot noise. Dark current is an undesirable leak current that is integrated as dark charges even when the subject image is not illuminated [12]. It is also referred to as reverse bias leakage current in non-optical devices and is present in all diodes. The amount of dark current is proportional to the integration time and is given by

$$N_{dark} = \frac{Q_{dark}}{q} = \frac{I_{dark} \cdot t_{int}}{q} \quad 2.4$$

and it is also related to the temperature.

Main source of dark current includes diffusion current of minority carriers under reverse bias, generation carriers in the bulk, and generated carriers at the surface.

For the minority carrier diffusion current, the diffusion current of electron from p-type substrate is dark current in the electron storage device. The current density is given by

$$J_{diff} = \frac{qD_n n_i^2}{L_n N_A} \quad 2.5$$

Here D_n and L_n are diffusion coefficient and diffusion length of electron, n_i and N_A are intrinsic carrier density and impurity concentration of the substrate, respectively.

The generation of carrier in the bulk occurs at the energy stated near mid-gap and the generation current is given by:

$$J_{gen} = \int_0^w g G dx \approx qGW = \frac{qn_i W}{\tau_g} \quad 2.6$$

where n_i , τ_g , G , and W are the intrinsic carrier density, generation carrier lifetime, generation rate variable from the Shockley-Read-Hall theory [13], [14], and width of depletion region, respectively.

Under the room temperature, the main factor of dark current is generation current at surface. That is because numerous traps exist at the interface of

Si-SiO₂. The current density of surface generation current is given by

$$J_{surf} = \frac{qS_0n_i}{2} \quad 2.7$$

Intrinsic carrier density n_i has a relationship with temperature T ,

$$n_i^2 \propto T^3 \exp\left(\frac{-E_g}{k_B T}\right) \quad 2.8$$

The rate of change in T^3 is larger than that of exponential T , that is the reason why dark current depends on the temperature.

Thermal noise

Thermal noise is the voltage fluctuation caused by the random Brownian motion of electrons in a resistive medium. The spectrum of thermal noise is proportional to the absolute temperature. If the resistance has a constant value R , the square of average voltage of thermal noise $\overline{v_n^2}$ can be written

$$\overline{v_{n,T}^2} = 4kTR \cdot \Delta f \quad 2.9$$

where k , T , and Δf are the Boltzmann constant, absolute temperature, and frequency bandwidth, respectively. The thermal noise was firstly measured by John B. Johnson at Bell Labs in 1926, and it was calculated according to the theory of Harry Nyquist, who was also at Bell Labs, so the thermal noise is also called Johnson-Nyquist noise [15][16]. The frequency spectrum of thermal noise is flat, that means thermal noise is white noise. The power spectral density of thermal noise S_{nt} is calculated by

$$S_{n,t} = \frac{\overline{v_n^2}}{\Delta f} = 4kTR \quad 2.10$$

The thermal noise in the channel of MOSFET can be described that when carriers move in the channel being scattered by the lattice and cause a small fluctuation in voltage. Because the resistance of the output cannot be infinite, a tiny fluctuation current can be detected, which is called channel current thermal noise.

When the drain source voltage V_{DS} equals zero, the channel can be treated as a homogeneous resistor. The noise in the channel is written by

$$i_d^2 = 4kTg_0 \quad 2. 11$$

where g_0 is the channel conductance at zero drain-source voltage. When the voltage $V_{DS} > 0$, the channel is not a homogeneous resistor anymore. To calculate the noise it must be split into small parts. The noise must be calculated in every one of those parts and then integrated along the whole channel.

In this condition, Equation 2. 11 becomes

$$i_d^2 = 4 \cdot k \cdot T \cdot \frac{\mu^2 \cdot W^2}{L^2 I_{DS}} \cdot \int_0^{V_{DS}} Q_n^2(V) dV \quad 2. 12$$

$$Q_n(x) = C_{ox} \cdot (V_{GS} - V_T(x) - V(x)) \quad 2. 13$$

The result of the integral equation is

$$I_d^2 = 8kT\mu C_{ox} \frac{W}{L} \cdot \frac{1}{(V_{GS} - V_T)} \times \left\{ (V_{GS} - V_T)^2 V_{DS} - (V_{GS} - V_T) V_{DS}^2 + \frac{1}{3} V_{DS}^3 \right\} \quad 2. 14$$

At the saturation point ($V_{DS} = V_{GS} - V_T$), we can simplify the equation to

$$I_d^2 = 4kT \cdot \frac{2}{3} \mu C_{ox} \frac{W}{L} (V_{GS} - V_T) = 4 \frac{2}{3} kT g_m \quad 2. 15$$

where μ , C_{ox} , V_T and g_m are electron mobility, oxide capacitance per unit area, threshold voltage, and conductance of saturation region, respectively.

Reset noise

Before the signal electrons are detected by the source follower from the floating diffusion (FD) region, the FD is reset to a reset voltage V_R . In this period, the voltage of floating diffusion is fluctuated by the thermal noise through the reset transistor. When the reset transistor is turned off, the noise

is sampled.

Figure 2. 6 shows the reset noise model while the floating diffusion is reset. In this case, the reset transistor is replaced by its on-resistor R_{ON} . The thermal noise power of the reset transistor is given by

$$\overline{v_{n,R}^2} = 4kTR_{ON} \quad 2. 16$$

This noise is afterwards sampled and held by the capacitor C_S . The reset noise power is given by integrating the thermal noise power by the transfer function over all frequencies. The reset noise power is given by

$$\overline{v_{n,R}^2} = \int_0^\infty 4kT \frac{R_{ON}}{1+(2\pi f R_{ON} C_S)^2} df = \frac{kT}{C_S} \quad 2. 17$$

The noise for electrons is also expressed by

$$\overline{Q_n^2} = \overline{v_{n,T}^2} C_S^2 = kT C_S \quad 2. 18$$

This is the reason why reset noise is also known as “kTC” noise.

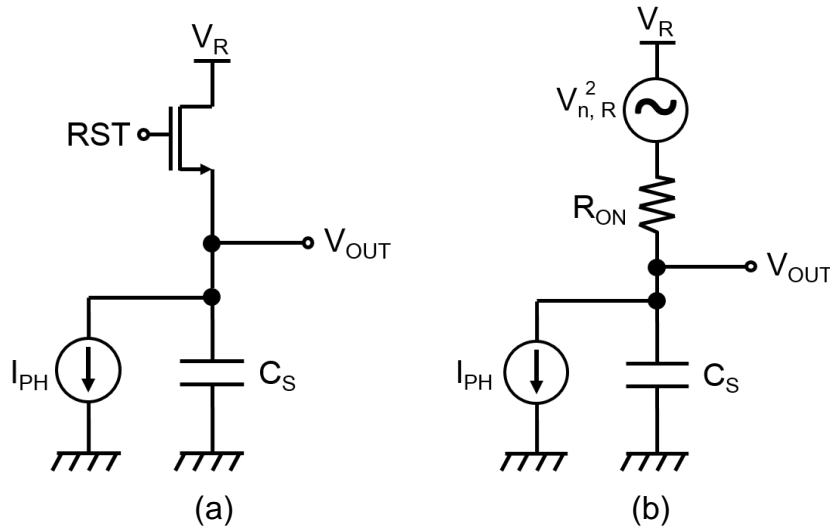


Figure 2. 6 Simplified circuit diagram of a pixel. (a) Schematic and (b) noise model.

1/f noise

1/f noise is a major noise source in CIS, it is also known as flicker noise. The noise spectrum of 1/f noise was firstly shown by McWhorter in 1955 [17].

In the MOS transistor, the current flows in the surface channel. The electron in channel is captured and emitted randomly by traps at the interface of Si and SiO₂, which causes a fluctuation in the amount of carriers in channel, and this is the source of 1/f noise. The noise power spectrum is inversely proportional to the frequency, when the transistor size is relatively large.

The power spectrum density of 1/f noise is given by

$$S_{n,f} = \frac{q^2 N_{ot}}{C_{ox}^2 A_G} \cdot \frac{1}{f} = \frac{N_f}{f} \quad 2. 19$$

where N_{ot} is effective trap density of 1/f noise, C_{ox} is the gate capacitance per unit area, and A_G is gate area.

The coefficient of 1/f noise N_f can be written

$$N_f = \left(\frac{q}{A_G C_{ox}} \right)^2 A_G N_{ot} \quad 2. 20$$

We can see that the $A_G N_{ot}$ equals the number of traps in channel. Think about only one trap in the channel, when the trap captures an electron, the generation of flat-band shift equals $q/(A_G C_{ox})$, and the noise power caused by one trap is proportional to $(q/(A_G C_{ox}))^2$. If the traps are independent each other, it is considered that the total noise power is proportional to $(q/(A_G C_{ox}))^2 \times A_G N_{ot}$.

When the size of transistor A_G , becomes smaller, the 1/f noise becomes larger, which is a large issue in CISs with the pixel size reduced. Especially, since the technologies have entered deep sub-micron region, the influence of one trap becomes dominant, and another noise, so-called random telegraph signal (RTS) noise appears in the current.

RTS noise

With the process scaling down, instead of the well-known 1/f noise, the RTS noise exhibits. As shown in Figure 2. 2, a trap is a localized energy state in the silicon band gap whose energy level is normally between the conduction band (E_c) and the valence band (E_v). Depending on the trap

energy level, its influence on CISs can be divided into two categories [18][19].

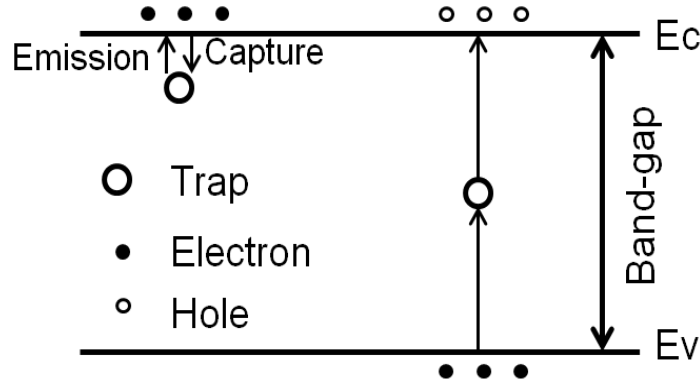


Figure 2. 7 Traps in the silicon band-gap.

If the trap energy is near E_c , it can interact with the carrier in the conduction band by capturing or releasing an electron, which introduces the RTS behavior.

When a trap is close to the middle of the band gap (mid-gap), the electrons in the valence band may gain enough energy and recombine with a hole. This process is called trap-assisted dark current.

The trap in mid-gap also introduces an RTS effect. However, because of the relatively large energy gap between mid-gap and E_c , the capture (or the emission process) may become slow. In CISs, the observed RTS noise is mainly due to the “fast” traps because of the high CDS frequency applied to the pixel output. The details of CDS will be discussed in next section. Thus, the majority of RTS traps observed from the test imager is expected to be close to the conduction band.

The power spectrum of RTS noise is given by

$$S_n(f) = \frac{4\tau_a^2 \overline{\Delta V^2}}{(\tau_c + \tau_e) \{1 + (2\pi f \tau_a)^2\}} \quad 2. 21$$

here

$$\frac{1}{\tau_a} = \frac{1}{\tau_c} + \frac{1}{\tau_e} \quad 2. 22$$

if $\tau_a = 0.5\tau_c = 0.5\tau_e$, Equation 2. 24 can be written

$$S_n(f) = \frac{4\tau_a \overline{\Delta V^2}}{1 + (2\pi f \tau_a)^2} \quad 2. 23$$

if $f \ll 1/2\pi\tau_a$, the power spectrum of RTS noise is flat, and if $f \gg 1/2\pi\tau_a$, the spectrum with an inverse proportion of f^2 .

2.3.2 Fixed Pattern Noise

The Fixed pattern noise (FPN) is described as the variation of the outputs from different pixels under the same illumination condition. Different from the random or temporal noise, it is fixed in space. The mismatch of in-pixel or column-level transistors, and the dark current generated inside the pixel are noise sources [20].

The device mismatch introduced during the fabrication process of in-pixel transistors induces the pixel-level FPN on images. The variations of the threshold voltage of the reset transistor, the input gate of the source follower amplifier, and charge injection from the reset transistor to the floating diffusion are noise sources. This noise can be cancelled by the use of the CDS technique [21].

The mismatch of the column circuitry in CMOS imagers will cause the column FPN on images. The threshold voltage variation caused by device mismatching during fabrication is the main noise source. The column FPN can be eliminated by subtracting the offset values measured in the dark condition.

2.4 Noise Reduction Techniques

2.4.1 Pinned Photodiode

The pinned photodiode (PPD) also be known as “buried photodiode”, which was firstly proposed by Noble for a MOS PPS to reduce dark current in 1968 [22]. In 1972, a buried channel CCD was introduced by Bell Labs to avoid the impact of interface traps [23]. The modern PPD structure was invented by Teranishi in 1982 to eliminate image lag in the interline-transfer CCD (ITCCD) [24]. In 1993, a CMOS image sensor with PPD was developed by Fossum to improve sensor performance [25].

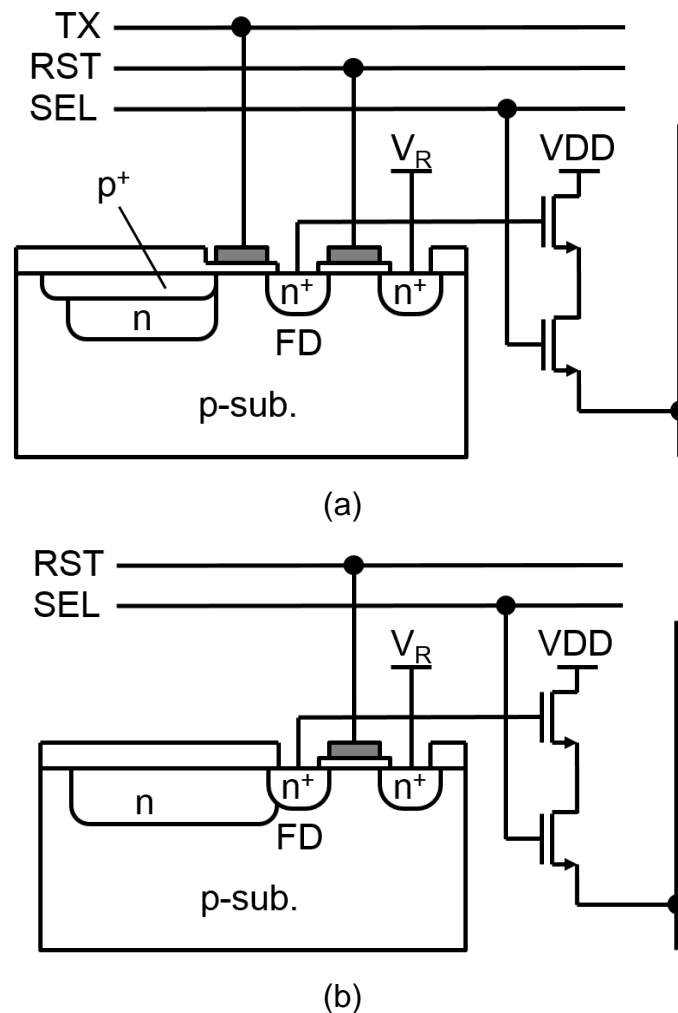


Figure 2. 8 Pixel structure of (a) 4-Tr. APS with pinned photodiode and (b) 3-Tr. APS with surface photodiode.

The structure of PPD is shown in Figure 2. 8 (a). In contrast with the

surface photodiode (SPD), which is shown in Figure 2. 8 (b), a shallow p+ layer is added. The PPD consists of two p-n junctions: the p+/n junction close to the surface and the n/p-well junction in the silicon bulk. Because of this p+ layer, the traps located at the interface of Si-SiO₂ are filled with holes. Even when the traps may capture electrons, it is easily recombined with holes because of existing high density holes. In addition, the contact area of PPD depletion region and semiconductor surface is reduced. Thus, the impact of the dominant dark current source, which is the trap at the interface of Si-SiO₂, is weakened.

2.4.2 CDS

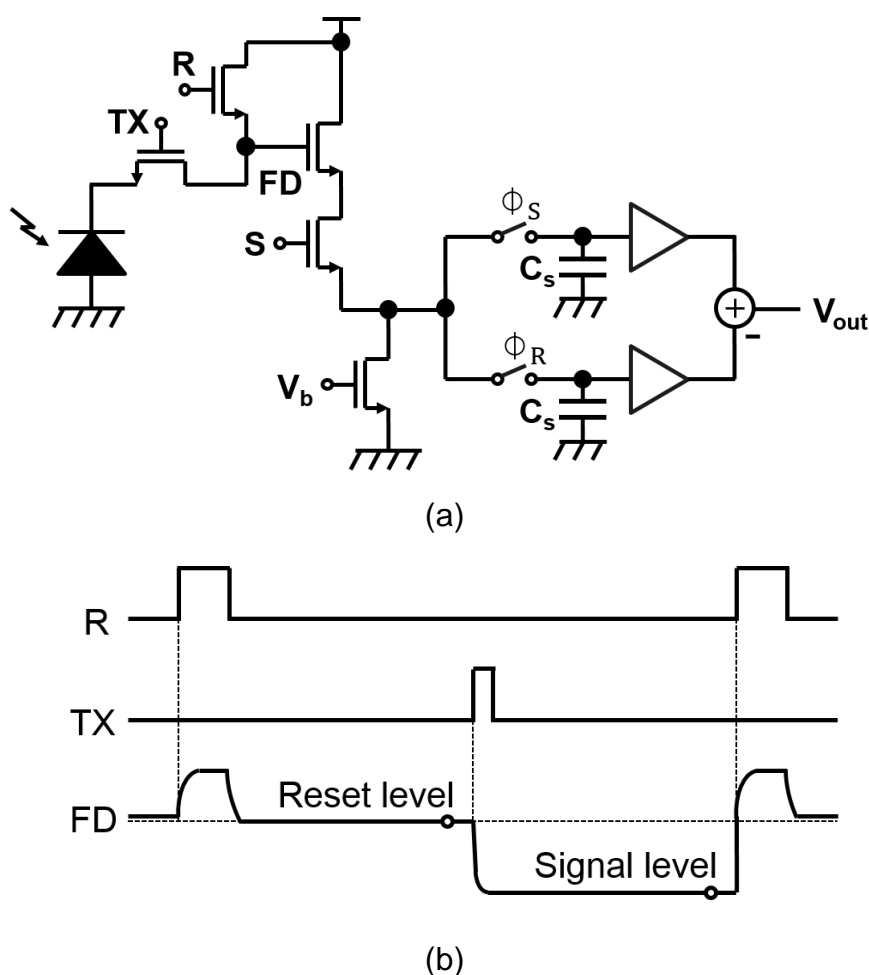


Figure 2. 9 Correlated double sampling. (a) Schematic diagram and (b) timing diagram.

The schematic and timing diagram of correlated double sampling (CDS) circuit is shown in Figure 2. 9, which consists of two sample and hold circuits.

When the select transistor S is turned on, this pixel is read out. Firstly, the FD is reset by turning on the reset transistor. When the reset transistor turns off, the reset noise is generated and stored in FD. The reset voltage is sampled and stored in capacity C_S by turning on the switch ϕ_R . When the transfer gate TX turns on, the electrons generated in PPD are transferred to FD. This time, switch ϕ_S turns on in turn to sample the signal voltage. The difference between the two samplings is figured out to obtain the output signal (V_{out}). In this processing, the same reset noise and FPN are sampled in both reset voltage and signal voltage. Finally, it is cancelled by taking the difference.

2.4.3 High-Gain Amplifier

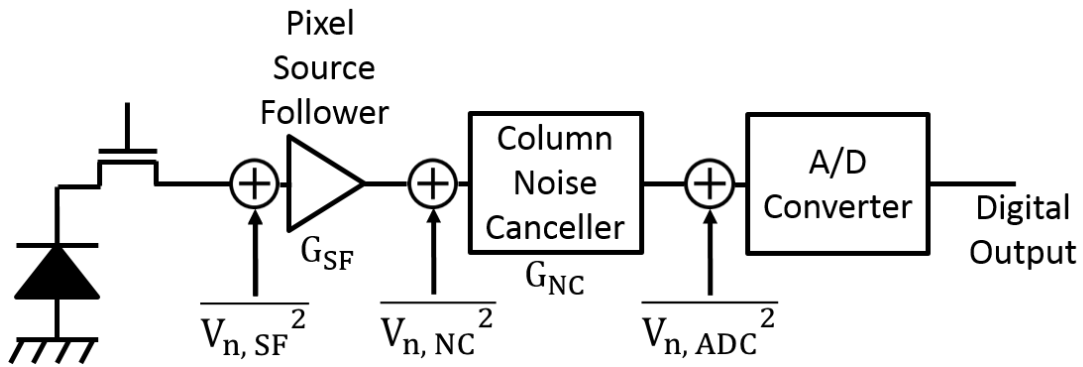


Figure 2. 10 Signal readout chain in CMOS image sensor.

Figure 2. 10 shows the signal readout chain of a CMOS image sensor with column ADC. Input referred noise of the source follower amplifier is expressed as

$$\overline{V_{n, IN}^2} = \overline{V_{n, SF}^2} + \frac{1}{G_{SF}^2} \left\{ \overline{V_{n, NC}^2} + \frac{1}{G_{NC}^2} \overline{V_{n, ADC}^2} \right\} \quad 2.24$$

where, $\overline{V_{n, SF}^2}$, $\overline{V_{n, NC}^2}$, and $\overline{V_{n, ADC}^2}$ are noise power of the in-pixel source follower amplifier, column noise canceller, and column ADC, respectively. G_{SF} and G_{NC} are gains of the in-pixel source follower amplifier and the column noise canceller, respectively. The column ADC eliminates the dominant wideband output buffer noise, which can be suppressed by increasing column noise canceller gain G_{NC} .

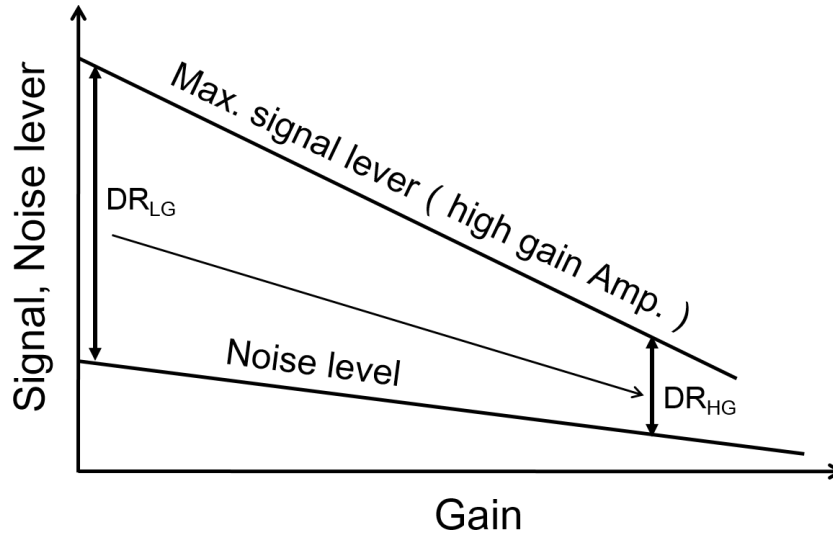


Figure 2. 11 Relationship between the gain and the noise level or maximum signal level.

A high gain column amplifier is effective for the readout circuit noise suppression [26]-[30]. However, not only the readout noise, but the effective input range are reduced by a high gain. Figure 2. 11 shows the relationship between the column gain and the noise level or maximum signal level. In other words, noise reduction effects of the high analog gain amplifier can be obtained by sacrificing the dynamic range. An adaptive gain technique is proposed for solving this problem [31]. But, in this case, the noise level and the dynamic range of imager are not sufficient [21].

2.4.4 CMS & Folding-Integration Technique

The CDS is widely used for noise cancelling in image sensors. An advanced noise reduction techniques, called correlated multiple sampling (CMS) is used in column parallel for readout noise reduction by high gain [32]-[37].

Figure 2. 12 (a) shows the schematic diagram of the CMS circuits which consists of a standard 4-Tr. active pixel structure, a switched capacitor integrator and sample and two hold circuits. Figure 2. 12 (b) shows the timing diagram of CMS. As shown in this diagram, reset and signal levels are sampled for M times and integrated in an SC integrator. Then, the amplified reset and signal levels are differentiated in analog or digital domain.

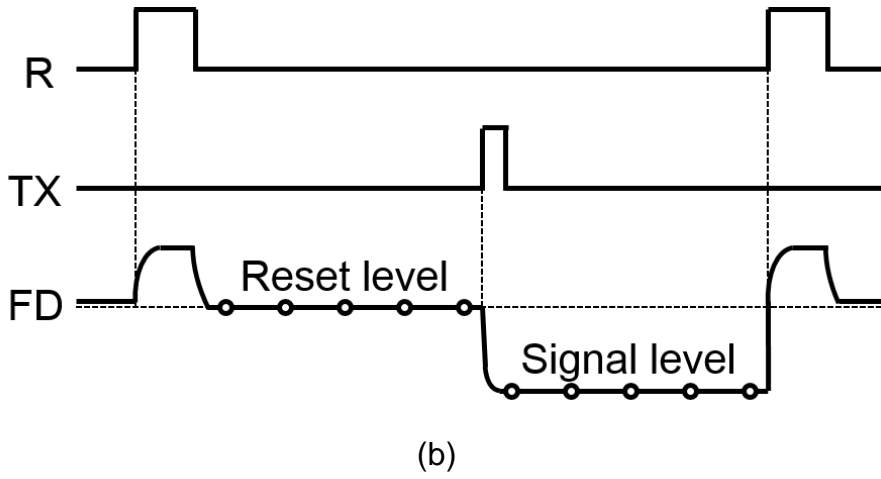
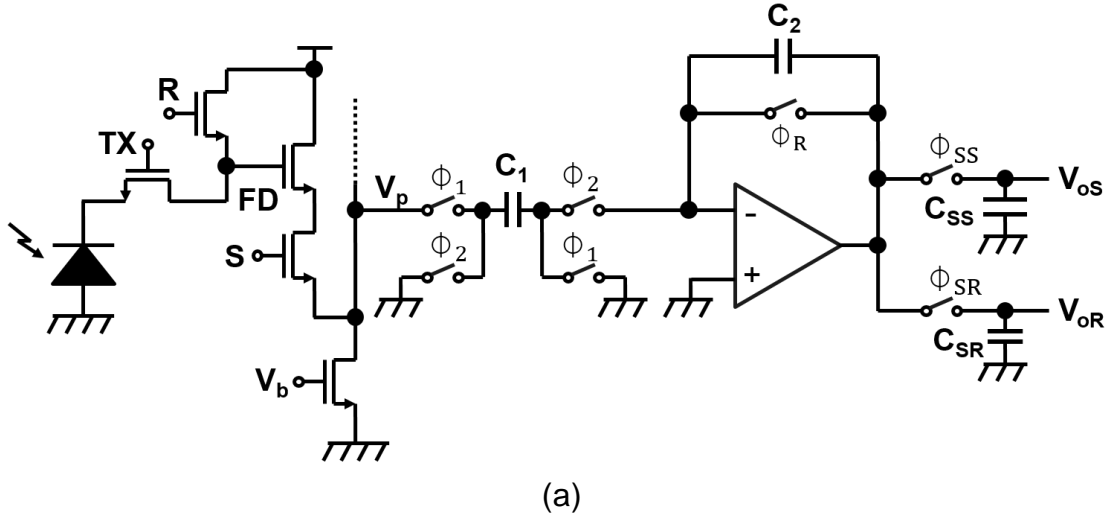


Figure 2. 12 Correlated multiple sampling. (a) Schematic diagram and (b) timing diagram.

The final output of the SC integrator with M times sampling in both reset and signal level is given by

$$\Delta V_O = \frac{C_1}{C_2} \sum_{i=1}^M \{V_{P,R}(i) - V_{P,S}(i)\} \quad 2. 25$$

If $C_1 = C_2$, the integrator output is written by

$$\overline{\Delta V_O} = M(\overline{V_{P,R}} - \overline{V_{P,S}}) \quad 2. 26$$

where $\overline{V_{P,R}}$ and $\overline{V_{P,S}}$ are average values of the reset and signal levels, respectively. In the CMS, the difference between the averages of reset and signal levels is amplified by a gain of M . Thus, not only the reset noise and

FPN can be cancelled, the circuit noise after CMS, such as sampling and hold circuits and ADC can be reduced by a factor of M .

However, the CMS circuits lead to a reduction of dynamic range, due to the linear region of amplifier used CMS is limited. Because the maximum output of CMS circuit ($\Delta V_{o,MAX}$) is constant, the maximum output of source follower become $\Delta V_{o,MAX}/M$ according to Equation 2. 26. It means that the output range of pixel source follower is reduced by increasing samplings. To maintain a high dynamic range the folding integration technique is presented [33][35].

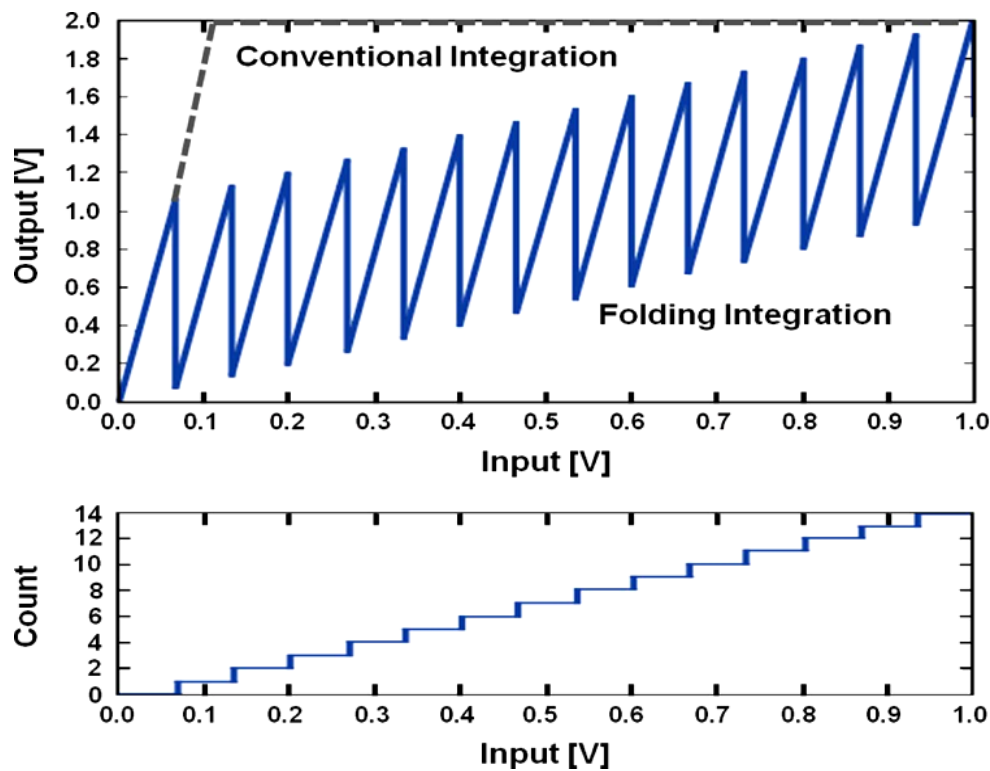


Figure 2. 13 Transfer curve of the folding integration ADC ($M=16$) [16].

Figure 2. 13 shows the characteristics of the folding integration. In this example $M = 16$, the output is folded 14 times and the counter output which shows the number of folds linearly increases as the input signal increases. In the conventional integration, the output increases linearly in small input signal region, and then saturates. In the folding integration, the analog signal amplitude is controlled to a limited range by the folding, while applying a high gain by the integration.

2.4.5 Buried n-Channel in-Pixel SF

As mentioned above, the dark current can be reduced by the pinned photodiode structure. The reset noise and FPN can be cancelled by CDS or CMS. Column readout noise can be suppressed by the high gain column amplifier. The dominant noise in CMOS image sensors becomes the in-pixel source follower $1/f$ or RTS noise. It has been proven that these kinds of noise are difficult to be reduced by circuit techniques. To eliminate these kinds of noise, a buried channel n-MOS transistor based in-pixel source follower was introduced [38]-[41].

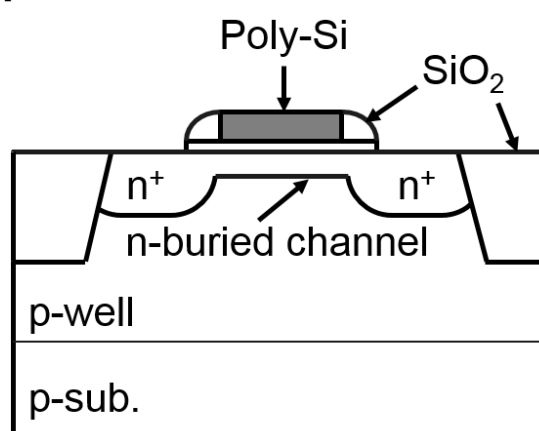


Figure 2. 14 Cross section of a buried channel n-MOS transistor.

The cross section of a buried channel n-MOS transistor is shown in Figure 2. 14. In the buried channel n-MOS transistor, an n-type doping along the channel of n-MOS transistor is introduced to lead the channel away from the Si-SiO₂ interface. Thus, the possibility of carriers be captured by traps at the Si-SiO₂ interface can be minimized. As a result, the $1/f$ and RTS noise can be greatly diminished. In addition, because of the negative threshold voltage of the buried channel transistor, which is caused by the n-type doping, the output swing of the pixel can be improved [18].

However, the transconductance (g_m) of the buried channel is almost half of that of the surface-mode device under the same gate bias condition. That is because the channel is buried into bulk silicon, thus reducing the gate modulation capability, which is an effect similar to increasing the gate oxide thickness [19]. As a result, the thermal noise is increased.

2.4.6 High Conversion Gain Pixel

In image sensors, the output of pixel is always an analog signal, which in most cases is an analog voltage. Thus, there is an important charge-to-voltage conversion process that takes place inside the pixels. The pixel conversion gain (CG) is the parameter which quantifies the efficiency of this process. The CG represents how much voltage change is produced by one electron at the output of the in-pixel source follower, which can be expressed as:

$$V_n = G_C \cdot N_n \quad 2. 27$$

where G_C is conversion gain.

Depending on the pixel architecture, the charge-to-voltage conversion process takes place at either the photo-sensing node or the charge-detection node. The conversion gain is mathematically defined as:

$$G_C = \frac{q}{C_{FD} + C_P} \cdot G_{SF} [\mu V/e^-] \quad 2. 28$$

where q is an electron charge, C_{FD} is the capacitance of the floating diffusion node, C_P is the parasitic capacitance connected to C_{FD} , and G_{SF} is the gain of the in-pixel source follower. The response linearity, uniformity, light sensitivity and random noise of the pixels are all influenced by the conversion gain value. The CG varies pixel to pixel. These characteristics also make the CG to be one of the most important parameters of a CMOS imager pixel.

Table 2. 1 Relationship between floating diffusion capacitance and conversion gain.

C_{FD}	$4fF$	$2.5fF$	$2fF$	$1fF$	$0.5fF$
G_C	$40 \mu V/e^-$	$64 \mu V/e^-$	$80 \mu V/e^-$	$160 \mu V/e^-$	$320 \mu V/e^-$

Table 2. 1 shows the relationship between FD node capacitance and CG. Where parasitic capacitance C_P is not considered, and source follower gain is assumed to 1. The smaller the FD capacitance, the larger the G_C .

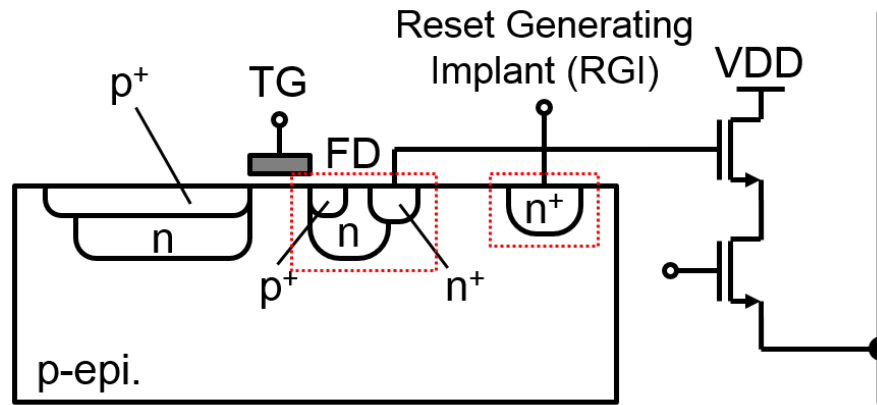


Figure 2. 15 Structure of a high conversion gain pixel.

As mentioned above, the noise of the pixel is influenced by CG. It means that the pixel noise can be reduced by increasing CG. To achieve a high CG, the parasitic capacitance of FD node should be minimized.

Figure 2. 15 shows a high conversion gain pixel structure [42]. In this pixel, two techniques are applied for FD parasitic capacitance reduction. The one method is placing a fully depleted diode structure between the TG and FD node to minimize the coupling capacitance generated between the TG and FD node [37]. The other one is removing the parasitic capacitance between FD node and reset gate by a reset-gate-less structure. In this structure, the pixel reset operation is implemented by applying a very high voltage (25V) on an implanted n^+ layer located close to the FD node. As a result, a low-noise ($0.27e^-$ at the peak of distribution) and high conversion gain ($220\mu V/e^-$) were achieved within $0.11\mu m$ CIS process [42].

Bibliography

- [1]. S. F. Yeh, K. Y. Chou, H. Y. Tu, C. Y. P. Chao, and F. L. Hsueh, "A 0.66e-rms temporal-readout-noise 3D-stacked CMOS image sensor with conditional correlated multiple sampling (CCMS) technique," in Symp. VLSI Circuits Digest of Technical papers, pp. C84–C85, Jun. 2015.
- [2]. S. Wakashima, F. Kusuvara, R. Kuroda, and S. Sugawa, "A linear response single exposure CMOS image sensor with 0.5e- readout noise and 76ke- full well capacity," in Symp. VLSI Circuits Digest of Technical papers, pp. C88–C89, Jun. 2015.
- [3]. S. K. Madan, B. Bhaumik, and J. M. Vasi, "Experimental observation of avalanche multiplication in charge-coupled devices," IEEE Transactions on Electron Devices, vol. 30, no. 6, pp. 694-699, Jun. 1983.
- [4]. J. Hynecek, "CCM-A new low-noise charge carrier multiplier suitable for detection of charge in small pixel CCD image sensors," IEEE Transactions on Electron Devices, vol. 39, no. 8, pp. 1972-1975, Aug. 1992.
- [5]. J. Hynecek, "Impactron-A New Solid State Image Intensifier," IEEE Transactions on Electron Devices, vol. 48, no. 10, pp. 2238-2241, Oct. 2001.
- [6]. P. A. Jerram, P. J. Pool, D. J. Burt, R. T. Bell, M. S. Robbins, "Electron Multiplying CCDs", SNIC Symposium, Apr. 2006.

- [7]. C. H. Sequin, F.J. Morris, T. A. Shankoff, M. F. Tompsett, and E.J. Zimany, "Charge-coupled area image sensor using three levels of polysilicon," *IEEE Transactions on Electron Devices*, vol. 21, no. 11, pp. 712-720, Nov. 1974.
- [8]. C. Niclass, A. Rochas, P. A. Besse, and E. Charbon, "Design and characterization of a CMOS 3-D image sensor based on single photon avalanche diodes," *IEEE Journal of Solid-State Circuits*, vol. 40, no. 9, pp. 1847-1855, Sep. 2005
- [9]. F. Villa, B. Markovic, S. Bellisai, D. Bronzi, A. Tosi, F. Zappa, S. Tisa, D. Durini, S. Weyers, U. Paschen, and W. Brockherde, "SPAD smart pixel for time of flight and time correlated single photon counting measurements," *IEEE Journal of Photonics*, vol. 4, no. 3, pp. 795-804, Jun. 2012.
- [10]. V. Agronskaia, L. Tertoolen, and H. C. Gerritsen, "Fast fluorescence lifetime imaging of calcium in living cells," *Journal of Biomedical Optics*, vol. 9, no. 6, pp. 1230-1237, Dec. 2004.
- [11]. M. Vitali, D. Bronzi, A. J. Krmpot, S. N. Nikolic, F. J. Schmitt, C. Junghans, S. Tisa, T. Friedrich, V. Vukojevic, L. Terenius, F. Zappa, and R. Rigler, "A single photon avalanche camera for fluorescence lifetime imaging microscopy and correlation spectroscopy," *IEEE Journal of Selected Topics in Quantum Electronics*, vol. 20, no. 6, pp. 344-353, Dec. 2014.
- [12]. Junichi Nakamura, "Image Sensors and Signal Processing for Digital Still Cameras," Taylor & Francis, 2006.
- [13]. R. N. Hall, "Electron-hole recombination in germanium," *Physical Review Letters*, vol. 87, no. 2, pp. 387, Jul. 1952.
- [14]. W. Shockley and W. T. Read, Jr., "Statistics of recombination of holes and electrons," *Physical Review Letters*, vol. 87, no 5, pp.

835-842, Sep. 1952.

- [15]. J. Johnson, "Thermal Agitation of Electricity in Conductors," Physical Review Letters, vol. 32, no. 1, pp. 97-109, Jul. 1928.
- [16]. H. Nyquist, "Thermal Agitation of Electric Charge in Conductors," Phys. Rev., vol. 32, no. 1, pp. 110-113, Jul. 1928.
- [17]. A. L. McWhorter, "1/f Noise and Related Surface Effects in Germanium," PhD dissertation, Massachusetts Institute of Technology, 1955.
- [18]. Xinyang Wang, "Noise in Sub-Micron CMOS Image Sensors," PhD dissertation, Delft Technology University, 2008.
- [19]. Yue Chen, "Low-Noise CMOS Image Sensors for Radio-Molecular Imaging," PhD dissertation, Delft Technology University, 2012.
- [20]. Sungho Suh, "A Study on Low Noise Wide Dynamic Range CMOS Image Sensors using Low Noise High Gain Readout Circuits," PhD dissertation, Shizuoka University, 2011.
- [21]. Min-Woong Seo, "A Study on Low-Noise High Dynamic Range High Resolution CMOS Image Sensors with Folding-Integration/Cyclic ADCs," PhD dissertation, Shizuoka University, 2012.
- [22]. P. J. W. Noble, "Self-scanned silicon image detector arrays," IEEE Transactions on Electron Devices, vol. 15, no. 4, pp. 202-209, Apr.1968.
- [23]. R. H. Walden, R. H. Krambeck, R. J. Strain, J. McKenna, N. L. Schryer, and G. E. Smith, "The buried channel charge-coupled device," Bell System Technical Journal, vol. 51, no. 7, pp. 1635-1640, Sep.1972.
- [24]. N. Teranishi, A. Kohono, Y. Ishihara, E. Oda, and K. Arai, "No image lag photodiode structure in the interline CCD image sensor," in Proc. IEDM, vol. 28, pp. 324-327, Dec. 1982.

- [25]. E. R. Fossum, "Active pixel sensors: are CCDs dinosaurs?" in Proc. SPIE CCD's and Solid State Optical Sensors III, vol. 1900, pp. 2-14, Jul. 1993.
- [26]. A. Krimski, N. Khaliullin, and H. Rhodes, "A $2e^-$ Noise 1.3 Mega Pixel CMOS Sensor," In Proc. IEEE Workshop CCD and Advanced Image Sensors, pp. 1–6, May 2003.
- [27]. S. Kawahito and N. Kawai, "Noise calculation model for high-gain column amplifiers of CMOS image sensor," in Proc. SPIE, vol. 5017, pp. 48-58, Jan. 2003.
- [28]. S. Kawahito, and N. Kawai, "Noise analysis of high-gain low-noise column readout circuits for CMOS image sensor," IEEE Transactions on Electron Devices, vol. 51, no. 2, pp. 185–194, Feb. 2004.
- [29]. N. Kawai, and S. Kawahito, "Measurement of low-noise column readout circuits for CMOS image sensors," IEEE Transactions on Electron. Devices, vol. 53, no. 7, pp. 1737–1739, Jul. 2006.
- [30]. P. Vu, B. Fowler, S. Mims, C. Liu, J. Balicki, H. Do, W. Li, and J. Appelbaum, "Low Noise High Dynamic Range 2.3 M pixel CMOS Image Sensor Capable of 100 Hz Frame Rate at Full HD Resolution," In Proc. International Image Sensor Workshop, pp. 161–164, Jun. 2011.
- [31]. M. Sakakibara, S. Kawahito, D. Handoko, N. Nakamura, H. Satoh, M. Higashi, K. Mabuchi, and H. Sumi, "A high-sensitivity CMOS image sensor with gain-adaptive column amplifiers," IEEE Journal of Solid-State Circuits, vol. 40, no. 5, pp. 1147–1156, May 2005.
- [32]. N. Kawai and S. Kawahito, "Effectiveness of a correlated multiple sampling differential average for reducing $1/f$ noise," IEICE Electronics Express, vol. 2, no. 13, pp. 379-383, Jul. 2005.

- [33]. S. Suh, S. Itoh, S. Aoyama, and S. Kawahito, "Column-parallel correlated multiple sampling circuits for MOS image sensors and their noise reduction effects," *Sensors*, vol. 10, 9139–9154, 2010
- [34]. Y. Chen, Y. Xu, A. J. Mierop, and Albert J. P. Theuwissen. "Column-parallel digital correlated multiple sampling for low-noise CMOS image sensors," *IEEE Sensors Journal*, vol. 12, no.4, pp. 793–799, Apr. 2012.
- [35]. M. W. Seo, S. Suh, T. Iida, T. Takasawa, K. Isobe, T. Watanabe, S. Itoh, K. Yasutomi, and S. Kawahito, "A low-noise high intrascene dynamic range CMOS image sensor with a 13 to 19b variable resolution column parallel folding-integration/cyclic ADC," *IEEE Journal of Solid-State Circuits*, vol. 47, no. 1, pp. 272–283, Jan. 2012.
- [36]. M. W. Seo, T. Sawamoto, T. Akahori, Z. Liu, T. Takasawa, T. Kosugi, T. Watanabe, K. Isobe, and S. Kawahito, "A low-noise high-dynamic range 17-b 1.3-Mpixel 30-fps CMOS image sensor with column-parallel two-stage folding-integration cyclic ADC," *IEEE Transactions on Electron. Devices*, vol. 59, no. 12, pp. 3396–3400. Dec. 2012.
- [37]. M. W. Seo, T. Sawamoto, T. Akahori, T. Iida, T. Takasawa, K. Yasutomi, and S. Kawahito, "A low noise wide dynamic range CMOS image sensor with low-noise transistors and 17b column-parallel ADC," *IEEE Sensors Journal*, vol. 13, no. 8, pp. 2922–2929. Aug. 2013.
- [38]. X. Y. Wang, P. R. Rao, and Albert, J. P. Theuwissen, "Characterization of buried channel n-MOST source followers in CMOS image sensor," *International Image Sensor Workshop*, pp. 223-225, Jun. 2007.

- [39]. X. Y. Wang, M. F. Snoeiij, P. R. Rao, A. J. Mierop, and Albert, J. P. Theuwissen, "A CMOS image sensor with a buried-channel source follower," International Solid-State Circuits Conference Dig. Tech., pp. 62-63, Feb. 2008.
- [40]. Y. Chen, X. Y. Wang, A. J. Mierop, and Albert, J. P. Theuwissen, "A CMOS image sensor with in-pixel buried channel source follower and optimized row selector," IEEE Transactions on Electron. Devices, vol. 56, no. 11, pp. 2390–2397. Nov. 2009.
- [41]. Y. Chen, Y. Xu, A. J. Mierop, X. Y. Wang, and Albert, J. P. Theuwissen, "A 0.7e-rms temporal readout noise CMOS image sensor for low light level imaging," International Solid-State Circuits Conference, pp. 384-386, Feb. 2012.
- [42]. M. W. Seo, S. Kawahito, K. Kagawa, and K. Yasutomi, "A $0.27e_{\text{rms}}^-$ read noise $220\mu\text{V}/e^-$ conversion gain reset gate less CMOS image sensor with $0.11\mu\text{m}$ CIS process," IEEE Electron Device Letters, vol. 36, no. 12, pp. 1344-1347, Dec. 2015.

Chapter 3

Noise Reduction by Multi-Aperture Imaging System with Selective Averaging

3.1 Introduction

Noise is one of the crucial elements which limits the performance of CMOS image sensor. Especially in low-light applications, the sensor noise such as dark current white defects and RTS noise becomes more visible. Since the active pixel sensor (APS) with pinned photodiode technology and the CDS technique were applied to CMOS image sensors in the mid 1990's, the reset noise and dark current in CMOS image sensor have been reduced significantly [1][2]. In the last two decades, many methods have been presented for low-noise CMOS image sensor design. High-gain amplifiers [3]-[6] for reducing readout circuits noise and amplifiers with multiple sampling [7]-[12] are effective for reducing thermal noise and 1/f noise of readout circuits. However, these high gain amplifiers are not useful for reducing the in-pixel random telegraph signal (RTS) noise and dark current shot noise.

RTS noise is described as a fluctuation in the current of a MOSFET [13] and it is generated by random capturing and emission of carriers in the

MOSFET channel at the traps of the silicon-silicon dioxide interface. The RTS noise in the CMOS image sensors is a major issue, especially in low-light conditions [14]. As the transistor is scaling down, the impurity concentration in the channel becomes non-uniform, and large RTS noise will appear [15]. The RTS noise can be reduced by the in-pixel buried channel source follower [16]-[19], in which an n-type doping along the channel of n-MOS transistor is introduced to lead the channel away from the Si-SiO₂ interface. Thus, the influence of traps near the interface is alleviated, which results in the 1/f and RTS noise reduction. However, the buried channel causes lower transconductance, which leads to larger thermal noise.

In this chapter, the RTS noise and dark current reduction based on a multi-aperture imaging system with a selective averaging method is presented. The multi-aperture system is composed of multiple components for both lens and sensor. In the proposed method, the multiple lenses are regarded as a synthetic single lens to collect more photons. The multiple pixels that correspond to a certain reproduced pixel are treated as sub-pixels. Namely, every virtual pixel is composed of real sub-pixels. Such redundancy is utilized to reduce the sensor noise. In the noise reduction method, the apertures are selected to minimize a combination variance of pixel value for each pixel in the dark condition. During capturing images, the pixel values among the selected apertures are averaged to calculate the pixel value of the reproduced image.

3.2 Multi-Aperture Imaging System

3.2.1 Structure of Multi-Aperture System

The most different feature of the multi-aperture imaging system compared with conventional single-aperture imaging systems is that multiple compact lenses and sensors in an $N \times N$ array are utilized. The schematic drawing of a multi-aperture imaging system is shown in Figure 1. 2. Note that one lens and one sensor constitute an aperture, which can be considered as a conventional single-aperture camera. In a single shot, multiple images are acquired simultaneously. The image size is typically the same for all apertures.

The multi-aperture imaging system or camera arrays has been used to boost the capabilities of conventional single-aperture imaging systems. Representative achievements are the synthesis of high dynamic range images [20], super-resolution and refocus [21], ultra-high-speed imaging [22], and system miniaturization [23].

In this work, a multi-aperture imaging system is used for noise reduction based on plurality of images acquired simultaneously. The images are combined into a single image using some noise reduction method, e.g., selective averaging, to improve the image quality in low-light conditions.

3.2.2 Merits of Multi-Aperture System

To increase the SNR of acquired images under low-light conditions for the given accumulation time determined by a frame rate, a smaller F-number lens is necessary. In the case of conventional single-aperture camera, large lens are needed to collect as much light as possible. To correct the lens aberration, more lens elements are required, so that the lens system will become very large and heavy. In the case of multi-aperture imaging system, however, it is possible to reduce size and weight of lens, as well as to increase image sensitivity by means of a lens array. The synthetic F-number

of multi-aperture imaging system can be obtained as $F_S = F_0/\sqrt{M}$, where F_0 is the F-number of each elemental lens, and M is the number of aperture. To show the effectiveness of the multi-aperture imaging system, it is compared with a single aperture counterpart shown in Figure 3. 1 (b). The single-aperture counterpart is an ideal conventional camera whose F-number is the same as the synthetic F-number of multi-aperture imaging system as shown in Figure 3. 1 (a). In the proposed noise reduction method, M pixels from all apertures are regarded as a sub-pixel, and they emulate a large pixel whose area is M times larger than that of the single aperture counterpart. Therefore, the number of pixels in the reproduced image out of the multi-aperture camera is as many as $N \times N$ although the number of physical pixels is $M \times N \times N$ in the proposed method.

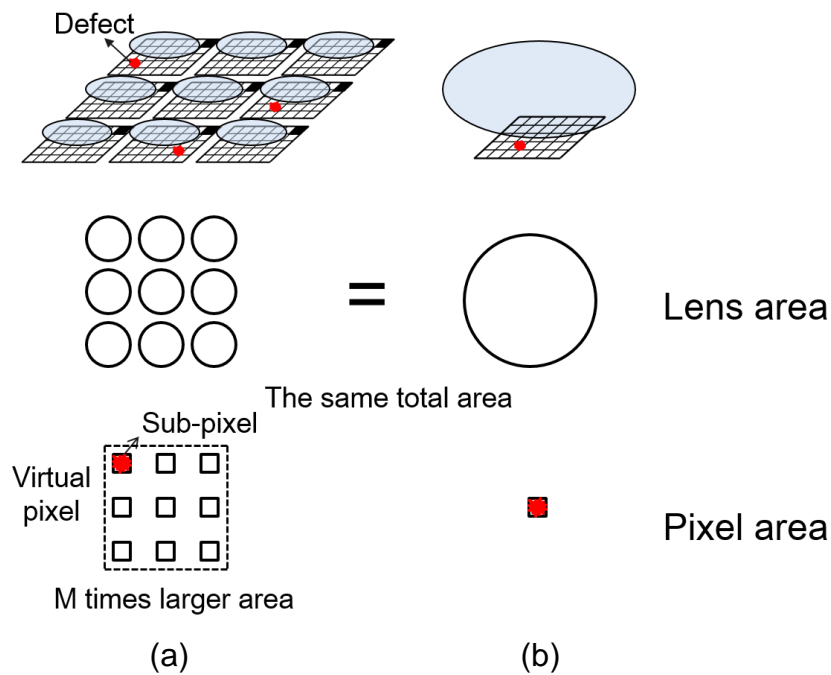


Figure 3. 1 Comparison of (a) multi-aperture imaging system and (b) single aperture counterpart.

Another virtue of the multi-aperture imaging system is that defect pixels are removed in the reproduced image without any interpolation. As shown in Figure 3. 1, in general, there are multiple malfunctioning pixels on a CMOS image sensor due to fabrication errors, which cause permanent dark, bright, or blinking dots in images, and degrade the image quality. In the multi-

aperture imaging system, there are multiple pixels ($N \times N$) for one identical objective point. If one aperture has a defective pixel, the pixels of the other apertures can be used to calculate the pixel value of the unified image.

In low-light conditions, because the signal level is very low, the RTS and dark current white defects become clearly visible, which seriously degrades the quality of image. Such large noise can be removed by the multi-aperture imaging system with a selective averaging method.

3.2.3 SNR Analysis in Multi-Aperture System

In this section, SNRs of the conventional single-aperture and multi-aperture imaging systems are compared based on a simple noise model. The SNR of conventional single-aperture imaging system, where sensor noise and photon shot noise are considered, is given by:

$$SNR_{SA} = 20 \log_{10} \frac{N_e}{\sqrt{\sigma_{sensor}^2 + N_e}} \quad 3.1$$

where, N_e is the number of signal electrons, σ_{sensor}^2 is a variance of the input referred sensor noise in electron.

In the multi-aperture imaging system, because multiple apertures are used, the SNR with summing up m apertures for averaging is given by:

$$SNR_{MA} = 20 \log_{10} \frac{m \cdot N_e}{\sqrt{m \cdot \sigma_{sensor}^2 + m \cdot N_e}} = 20 \log_{10} \frac{\sqrt{m} \cdot N_e}{\sqrt{\sigma_{sensor}^2 + N_e}} \quad 3.2$$

The signal electrons number, N_e has a relationship with illumination and some other parameters, which is given by:

$$N_e = \alpha \cdot \eta \cdot A \cdot \frac{RT}{4F_n^2} \cdot E_0 \cdot \tau \quad 3.3$$

where α is a proportional constant, η is the quantum efficiency, which is the ratio of the number of generated electrons to the number of incident photons, A is pixel area, R is object reflectivity, T is lens transmittance, F_n is F-

number of a single aperture, which is calculated by the ratio of focal length f to aperture diameter D , E_0 is illumination on the object surface, and is exposure time.

To simplify the equation, we define the product of the α , η , R , T , E_0 and τ as a constant C . Therefore, the Equation 3. 3 is expressed as:

$$N_e = C \cdot \frac{A}{F_n^2} \quad 3. 4$$

By combining Equation 3. 4 and 3. 2, the following equation becomes,

$$SNR_{MA} = 20 \log_{10} \frac{\sqrt{M \cdot C \cdot A / F_n^2}}{\sqrt{\sigma_{sensor}^2 + C \cdot A / F_n^2}} \quad 3. 5$$

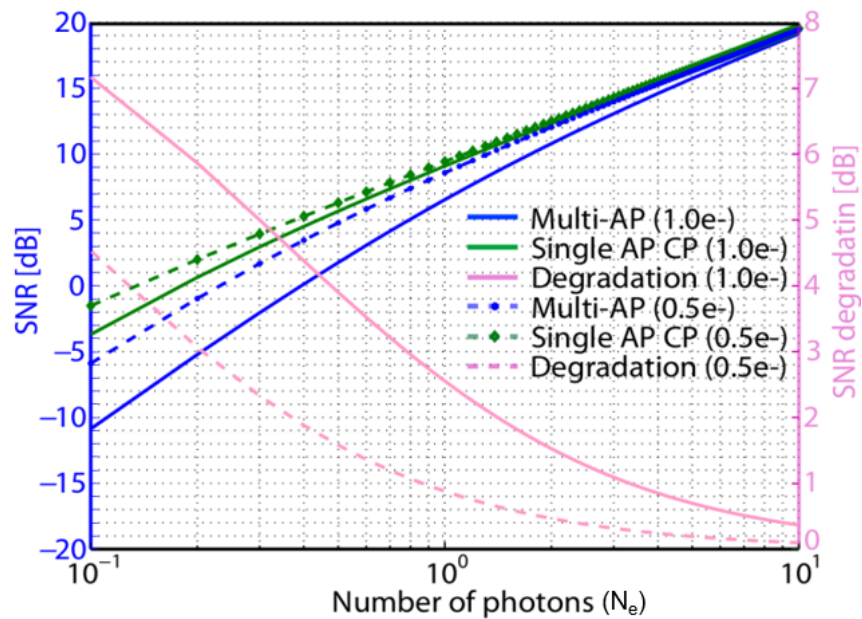
Equation 3. 5 shows the relationship between SNR, pixel area, and F-number. To increase the SNR, the F-number should be reduced or the pixel area increased. If we reduce the F-number, the diameter of the aperture should increase. However, in fact, it is not easy to realize a compact and fast lens with a high spatial resolution. Another way to increase the SNR is to increase the pixel area. When the field of view is fixed, this option requires a larger image circle, which does not mean to require a high spatial resolution, but to make the lens bigger and heavier. Therefore, in the camera design, taking the balance of pixel area and F-number is crucial.

To compare the performance of the single-aperture and multi-aperture cameras, the multi-aperture camera should be compared with its single aperture counterpart shown in Figure 3. 2(b) , which has the same F-number as that of the synthetic F-number of the multi-aperture camera. The SNR of the single aperture counterpart is written by:

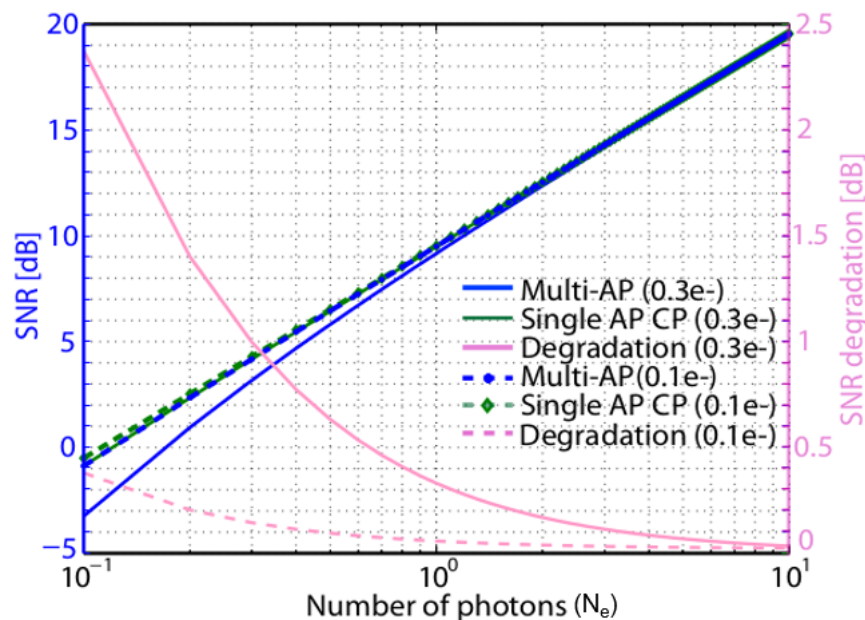
$$SNR_{SACP} = 20 \log_{10} \frac{M \cdot N_e}{\sqrt{\sigma_{sensor}^2 + M \cdot N_e}} \quad 3. 6$$

The signal levels are the same for the multi-aperture system and the single aperture counterpart when $m = M$. However, the noise factor in Equation 3.

2 is m times as large as that in Equation 3. 6, which is caused by the number of physical pixels related to a single reproduced pixel. The sensor noise (σ_{sensor}) is summed up among m pixels in the multi-aperture imaging system. On the other hand, in the single aperture counterpart, only one sensor is used, so the noise factor is unity when we assume that the sensor noise of single aperture counterpart and that of each aperture are the same.



(a)



(b)

Figure 3. 2 SNRs for different values of amplifier noise. (a) $1.0e^-$ and $0.5e^-$. (b) $0.3e^-$ and $0.1e^-$. (AP: aperture, CP: counterpart)

Figure 3. 2(a) shows the calculation results of SNR of multi-aperture and single aperture counterpart when the number of apertures is 9 ($m = 9$), and the number of photons (N_e) varies from 10^{-1} to 10^1 for the sensor noise (σ) of $1.0e^-$ and $0.5e^-$. The SNR of the multi-aperture is obviously smaller when the number of photons is below 10^1 . The degradation is shown by the difference between the SNRs for the multi-aperture and the single aperture counterpart. Because the noise power of the multiple apertures is summed up, the SNR for the multi-aperture camera is smaller than that for the single aperture counterpart. As the number of photons is increased, the photon shot noise also increases. Because the level of the sensor noise is independent of the incident light intensity and the photon shot noise becomes the dominant noise when incident light is strong enough, the effect of sensor noise can be negligible in SNR calculation. So the SNR of multi-aperture can be considered to be almost the same as that of the single aperture counterpart when the number of photons is larger than 10^1 .

Although the SNR of multi-aperture is degraded when compared with the single aperture counterpart, the degradation can be reduced by reducing the sensor noise. Figure 3. 2(b) shows the calculated SNRs for smaller sensor noise such as $0.3e^-$ and $0.1e^-$. When the sensor noise is less than $0.3e^-$, the SNRs of multi-aperture and single aperture counterpart can be considered to be almost the same even in the very low light conditions

3.3 Selective Averaging

In the multi-aperture imaging system, $N \times N$ images for one picture are acquired simultaneously. However, the pixel values for an identical objective point are not exactly the same, because different random noise of pixel amplifier and ADC is added to each of them.

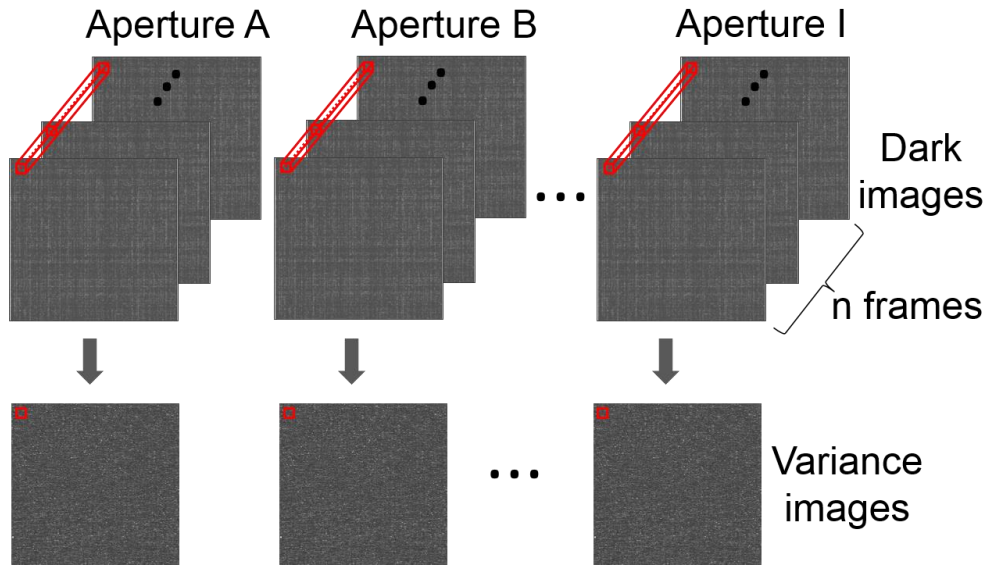


Figure 3. 3 Variance calculations in multi-aperture camera.

Figure 3. 3 shows the variance calculation in the multi-aperture imaging system, where n -frame images are captured in a dark condition. Obviously, there are $N \times N$ variances for one objective point and the values of variance in the apertures are different pixel to pixel. The variances are sorted from the minimum to the maximum for each pixel, and then a combination variance is calculated by using the following equation:

$$S_m^2 = \frac{1}{m^2} \sum_{i=1}^m \sigma_i^2 \quad 3.7$$

here, m is the number of selected apertures, σ_i^2 is a sorted variance, and S_m^2 is the combination variance.

The sorting process is to find the smallest combination variance among the apertures. After combination variances calculation, the minimum one is found out to determine the selected apertures. Generally, as m increases,

the combination variance becomes smaller according to the factor of $1/m^2$, when the variances are comparable. Sometimes pixels have very large noise due to RTS noise or shot noise of large dark current, so that the variance of these pixels will be very large. If the variance is relatively large, the combination variance for $(m + 1)$ apertures can be larger than the combination variance for m apertures. Thus, pixels with large noise are automatically excluded.

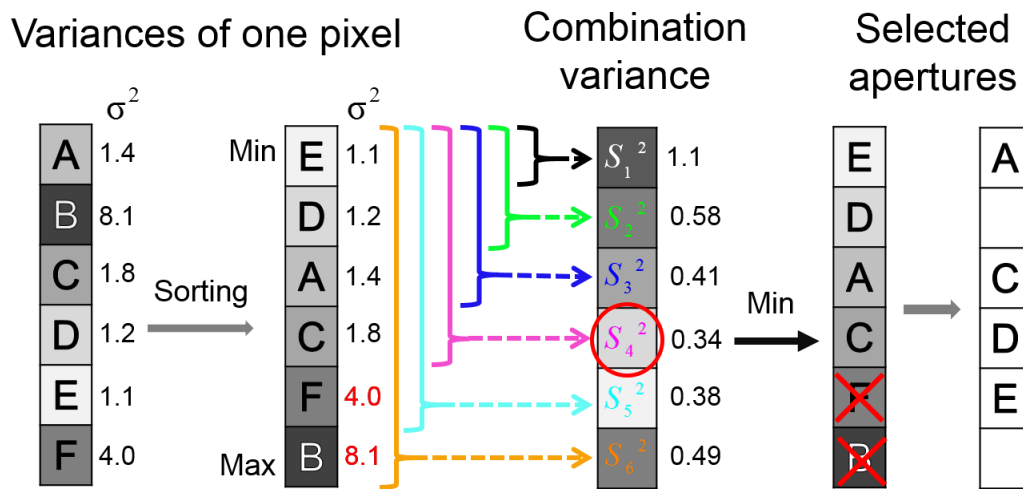


Figure 3. 4 Procedure of aperture selection for one pixel.

Figure 3. 4 shows an example of aperture selection at one pixel. The variance in aperture B and F are larger than the others, and it causes that the combination variances S_6^2 and S_5^2 are larger than S_4^2 . Thus, the minimum combination variance is found out to be S_4^2 , and the apertures used to calculate the minimum combination variance can also be determined as A, C, D, and E. Those apertures are the selected apertures for this pixel. In image shooting, the pixel values among the selected apertures are averaged, and the averaged value is defined as the pixel value of the unified virtual image. Because averaging is operated only to the selected apertures, this method is called selective averaging. When the RTS noise and the shot noise caused by dark current are very large, it causes a large variance. In this method, the apertures that have a large variance will not be selected, so these noise components can be removed.

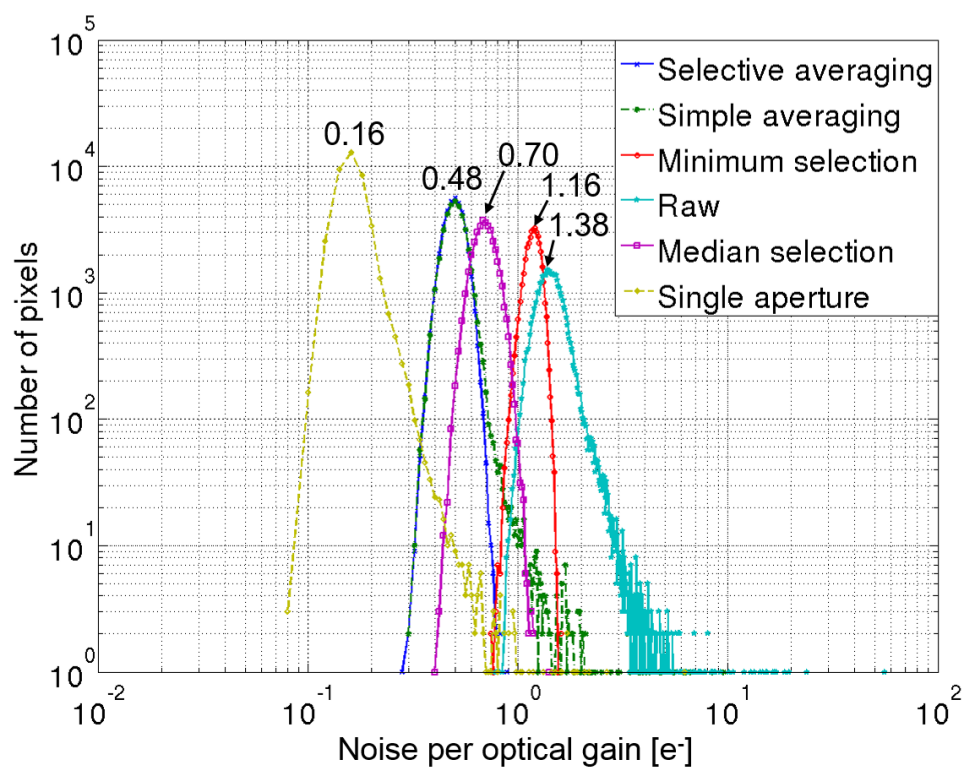
The selected apertures are determined only by the variance of pixel in dark, namely sensor noise. Even the objects change, if the distance and the sensor noise do not significantly change, the selected apertures for each pixel are invariable. For some of the dark or bright defect pixels, the pixel values can be continuously very small or large, respectively, but the variance is small. Such situation can happen when the pixel source followers do not work correctly. If the selective averaging method is applied directly, these pixel values of the reproduced image will be deteriorated. In this situation, thresholding is effective. If the minimum pixel value for n -frame images (Figure 3. 3) is larger than the threshold or pixel value is insensitive to light, we assign a huge number to the variance of these defect pixels, so that those will not be selected.

3.4 Simulation Results

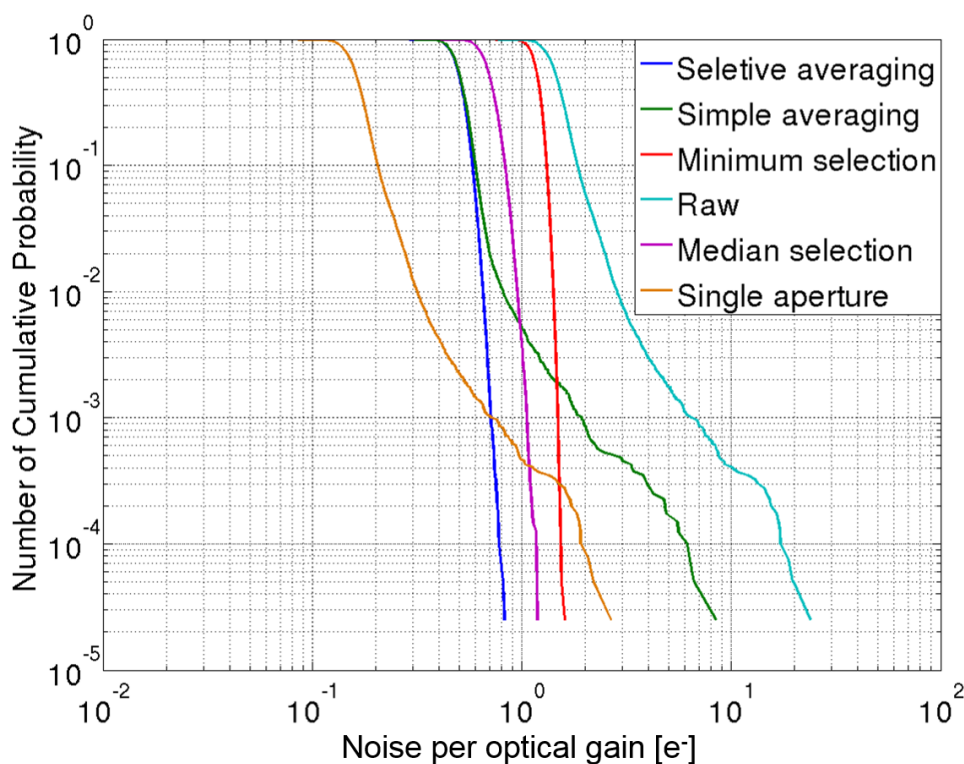
In simulation, the selective averaging method is compared with the single aperture counterpart, one extracted image among the multi-aperture images (referred as “raw”), and some other processing methods in the multi-aperture system such as simple averaging, minimum noise selection, and median selection. In the simple averaging, no selection is done. All the apertures are used to take average. Minimum selection means that the aperture with the minimum variance is selected for every pixel, and the pixel value of the selected sub-pixel is copied to the final reproduced image. In median selection, the median pixel value among the multiple sub-pixels is selected for every pixel.

To compare six cases, the resultant noise is normalized by optical gain. The optical gain is introduced to compare the S/Ns of different optical configurations and processing methods. Here, optical gain is defined by the ratio of the number of incident photons, namely effective pupil area, based on that of “raw”. The optical gains for raw, minimum selection, and median selection are all 1 because the pixel value of only one aperture is used. The optical gain for the simple averaging is M , which is the same as the number of apertures. For the single aperture counterpart, although, only one sensor is used, the F-number of single aperture counterpart is the same as that of the multi-aperture system. Therefore, the number of signal electrons should be the same for the single aperture counterpart and the multi-aperture system. So the optical gain of single aperture counterpart is M . In the selective averaging, the optical gain depends on the number of selected apertures, and varies from 1 to M .

Figure 3. 5 shows the noise distribution of all methods. The peak noise levels for the selective averaging and the simple averaging are the same and smaller than the minimum selection and the raw. However, in the simple averaging method, the large noise tailing such as RTS noise and dark current



(a)



(b)

Figure 3. 5 Noise distributions for different methods. (a) Histogram and (b) cumulative probability.

shot noise cannot be removed because they are included in averaging. While the large noise tailing is reduced by the median selection and minimum selection methods, the peak noise levels are larger than that of selective averaging due to unity optical gain. The selective averaging method shows the smallest peak noise among several methods except the single aperture counterpart and no large noise tailing is observed, which means that the large RTS noise and dark current shot noise are removed.

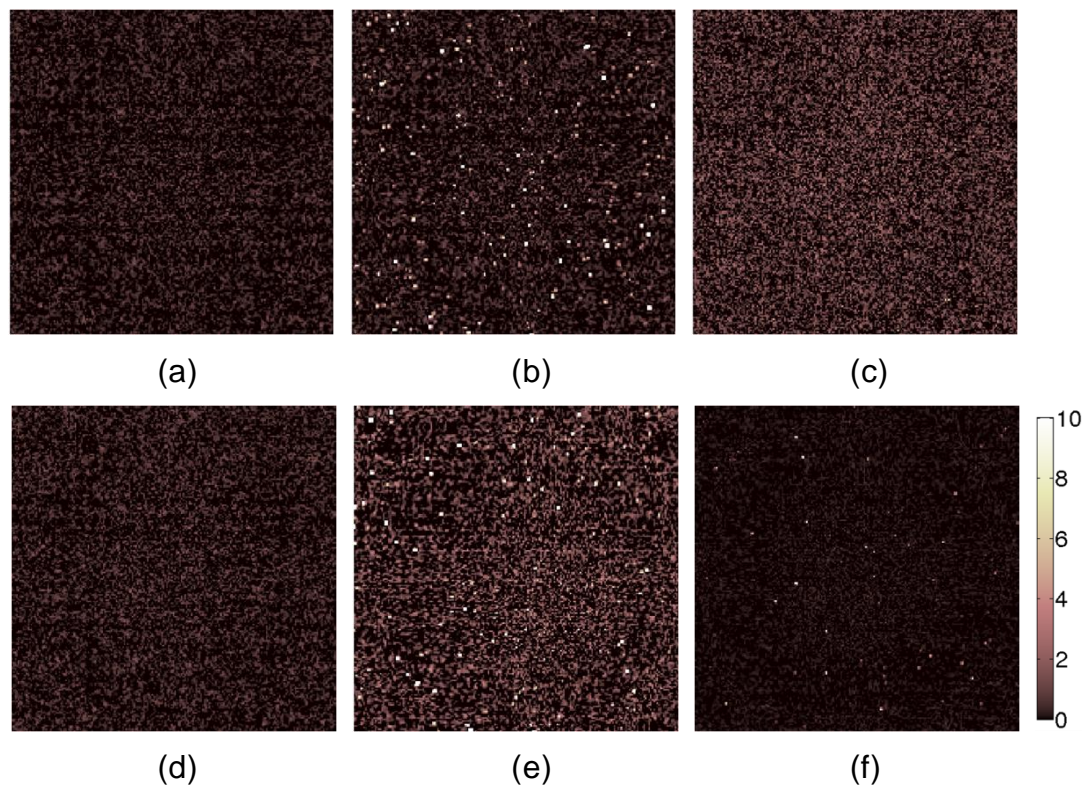


Figure 3. 6 Dark image for different methods. (a) Selective averaging, (b) simple averaging, (c) minimum selection, (d) median selection, (e) raw, and (f) single aperture counterpart.

Figure 3. 6 shows the resultant images in the dark. The white spots represent the RTS noise or large dark current white defects. The larger the noise is, the brighter the spot is. As mentioned above, the raw image shows the original sensor noise level. The others show the noise in the reproduced images, where the sensor noise is the same. The noise of the raw shows the highest level, and tailing in the right side in Fig. 3.5 is caused by the RTS noise and dark current shot noise. Because of the optical gain of 9 and the

sensor noise gain factor of unity which is the same as “raw”, the noise for the single aperture counterpart becomes the smallest when the noise is divided by the optical gain.

Future CMOS image sensors with much smaller transistors will show much larger RTS noise, so that the noise tailing in Fig. 3.5 for the single aperture counterpart will spread more widely beyond the noise distribution of the selective averaging. Although the peak noise of the single aperture counterpart is the smallest, there are pixels with larger noise than in the selective averaging, the median selection, and the minimum selection. Therefore, it will be expected that the selective averaging method can give the best image quality in future CMOS image sensors.

3.5 Summary

In this chapter, a multi-aperture imaging system, which is composed of multiple components for both lens and sensor, for increasing optical gain, and selective averaging, which removes the RTS noise and the dark current white defects by minimizing the synthetic sensor noise at every pixel, is proposed. In low-light conditions, the quality of simultaneously captured multiple images are very low due to visible noise. An enhanced image can be reproduced by averaging only in selected apertures. The selected apertures are determined by a minimized combination variance which is calculated by the variance of dark pixel value. It is verified by simulation that the effective noise normalized by optical gain in the peak of noise histogram is reduced from $1.38e^-$ to $0.48e^-$ in a 3×3 -aperture system.

Bibliography

- [1]. E. R. Fossum, "Active pixel sensors: Are CCD's dinosaurs," In Proc. SPIE Charge Coupled Devices Solid State Optical Sensors III, vol. 1900, pp. 2–14, Jul. 1993.
- [2]. P. P. K. Lee, R. C. Gee, R. M. Guidash, T. H. Lee, and E. R. Fossum, "An active pixel sensor fabricated using CMOS/CCD process technology," in Proc. IEEE Workshop CCDs and Advanced Image Sensors, pp. 115-119, Apr. 1995.
- [3]. A. Krimski, N. Khaliullin, and H. Rhodes, "A $2e^-$ Noise 1.3 Mega Pixel CMOS Sensor," In Proceedings of the IEEE Workshop CCDs and Advanced Image Sensors, pp. 1–6, May 2003.
- [4]. S. Kawahito, and N. Kawai, "Noise calculation model for high-gain column amplifiers of CMOS image sensor," in Proc. SPIE, vol. 5017, pp. 48-58, May 2003.
- [5]. S. Kawahito, and N. Kawai, "Noise analysis of high-gain low-noise column readout circuits for CMOS image sensor," IEEE Transactions on Electron Devices, vol. 51, no. 2, pp. 185–194, Feb. 2004.
- [6]. P. Vu, B. Fowler, S. Mims, C. Liu, J. Balicki, H. Do, W. Li, and J. Appelbaum, "Low Noise High Dynamic Range 2.3 M pixel CMOS Image Sensor Capable of 100 Hz Frame Rate at Full HD Resolution," In Proceedings of International Image Sensor Workshop, pp. 161–164, Jun. 2011.

- [7]. N. Kawai, and S. Kawahito, "Effectiveness of a correlated multiple sampling differential average for reducing $1/f$ noise," IEICE Electronics Express, vol. 2, no. 13, pp. 379-383, Jul. 2005.
- [8]. S. Suh, S. Itoh, S. Aoyama, and S. Kawahito, "Column-parallel correlated multiple sampling circuits for MOS image sensors and their noise reduction effects," Sensors, vol. 10, 9139–9154, 2010
- [9]. Y. Chen, Y. Xu, A. J. Mierop, and Albert J. P. Theuwissen, "Column-parallel digital correlated multiple sampling for low-noise CMOS image sensors," IEEE Sensors Journal, vol. 12, no.4, pp. 793–799, Apr. 2012.
- [10]. M. W. Seo, S. Suh, T. Iida, T. Takasawa, K. Isobe, T. Watanabe, S. Itoh, K. Yasutomi, and S. Kawahito, "A low-noise high intrascene dynamic range CMOS image sensor with a 13 to 19b variable resolution column parallel folding-integration/cyclic ADC," IEEE Journal of Solid-State Circuits, vol. 47, no. 1, pp. 272–283, Jan. 2012.
- [11]. M. W. Seo, T. Sawamoto, T. Akahori, Z. Liu, T. Takasawa, T. Kosugi, T. Watanabe, K. Isobe, and S. Kawahito, "A low-noise high-dynamic range 17-b 1.3-Mpixel 30-fps CMOS image sensor with column-parallel two-stage folding-integration cyclic ADC," IEEE Transactions on Electron Devices, vol. 59, no. 12, pp. 3396–3400. Dec. 2012.
- [12]. M. W. Seo, T. Sawamoto, T. Akahori, T. Iida, T. Takasawa, K. Yasutomi, and S. Kawahito, "A low noise wide dynamic range CMOS image sensor with low-noise transistors and 17b column-parallel ADC," IEEE Sensors Journal, vol. 13, no. 8, pp. 2922–2029. Aug. 2013.
- [13]. A. Konczakowska, J. Cichosz, and A. Szewczyk, "A new method for

- identification of RTS noise,” Bulletin of the Polish Academy of Sciences Technical Sciences, vol. 54, no. 4, pp. 457–460, 2006.
- [14]. C. Leyris, F. Martine, M. Valenza, A. Hoffmann, J. C. Vildeuil, F. Roy, “Impact of Random Telegraph Signal in CMOS Image Sensors For Low-Light Levels,” In Proc. 32nd European Solid-State Circuits Conference, pp. 376–379, Sep. 2006.
- [15]. K. Takeuchi, “Impact of discrete-change-induced variability on scaled MOS devices,” IEICE Transactions on Electronics, vol. E95-C, no. 4, pp. 414–420, Apr. 2012.
- [16]. X. Y. Wang, P. R. Rao, and Albert, J. P. Theuwissen, “Characterization of buried channel n-MOST source followers in CMOS image sensor,” International Image Sensor Workshop, pp. 223-225, Jun. 2007.
- [17]. X. Y. Wang, M. F. Snoeij, P. R. Rao, A. J. Mierop, and Albert, J. P. Theuwissen, “A CMOS image sensor with a buried-channel source follower,” International Solid-State Circuits Conference Digest of Technical, pp. 62-63, Feb. 2008.
- [18]. Y. Chen, X. Y. Wang, A. J. Mierop, and Albert, J. P. Theuwissen, “A CMOS image sensor with in-pixel buried channel source follower and optimized row selector,” IEEE Transactions on Electron Devices, vol. 56, no. 11, pp. 2390–2397. Nov. 2009.
- [19]. Y. Chen, Y. Xu, A. J. Mierop, X. Y. Wang, and Albert, J. P. Theuwissen, “A 0.7e-rms temporal readout noise CMOS image sensor for low light level imaging,” International Solid-State Circuits Conference, pp. 384-386, Feb. 2012.
- [20]. B. Wilburn, N. Joshi, V. Vaish, E.-V. Talvala, E. Antunez, A. Barth, A. Adams, M. Horowitz, and M. Levoy, “High performance imaging using large camera arrays,” ACM Transactions on Graphics, vol. 24,

no. 3, pp. 765–776, Jul. 2005.

- [21]. K. Venkataraman, D. Lelescu, J. Duparre, A. McMahon, G. Molina, P. Chatterjee, R. Mullis, and S. Nayar, “Picam: An ultra-thin high performance monolithic camera array,” *ACM Transactions on Graphics*, vol. 32, no. 6, pp. 1–13, Nov. 2013.
- [22]. F. Mochizuki, K. Kagawa, S. ichiro Okihara, M.-W. Seo, B. Zhang, T. Takasawa, K. Yasutomi, and S. Kawahito, “Single-shot 200Mfps 5×3 -aperture compressive CMOS imager,” *International Solid-State Circuits Conference*, pp. 1–3, Feb. 2015.
- [23]. J. Tanida, T. Kumagai, K. Yamada, S. Miyatake, K. Ishida, T. Morimoto, N. Kondou, D. Miyazaki, and Y. Ichioka, “Thin observation module by bound optics (tombo): concept and experimental verification,” *Applied Optics*, vol. 40, no. 11, pp. 1806–1813, Apr. 2001.

Chapter 4

Implementation of 3×3 -Aperture Monochrome Camera with Selective Averaging

4.1 Introduction

Imaging in low-light conditions is a very important task in broadcasting, digital cinemas, surveillance, and so on. Recent progress of low-noise CMOS image sensors [1]-[5] have contributed to such applications. However, small defects, which can be neglected in moderate applications, are emphasized because the number of incident photons on pixel is very few in extremely low-light conditions. RTS noise and shot noise by large dark current are major factors of abnormally large noise [6]-[8]. These kinds of noise are difficult to be reduced by circuit techniques. Increasing exposure time is a way to increase SNR of image in low-light conditions, but it sacrifices the time resolution (or frame rate), which will result in image blur in moving scenes. Although the F-number of imaging lens can be reduced by collecting more photons, it increases the aberration of the lens or the size and weight.

The multi-aperture imaging system which increases the optical gain with a lens array and the selective averaging which removes the RTS noise and

large dark current shot noise meet the requirements of image quality enhancement in low-light conditions.

A prototype 3×3 -aperture monochrome camera is developed to demonstrate the low-noise performance [10]. In this chapter, the structure and the image reproduction procedure of the multi-aperture camera are introduced. The low-noise performance which is demonstrated by experiment is discussed.

4.2 3×3 Multi-Aperture Monochrome Camera

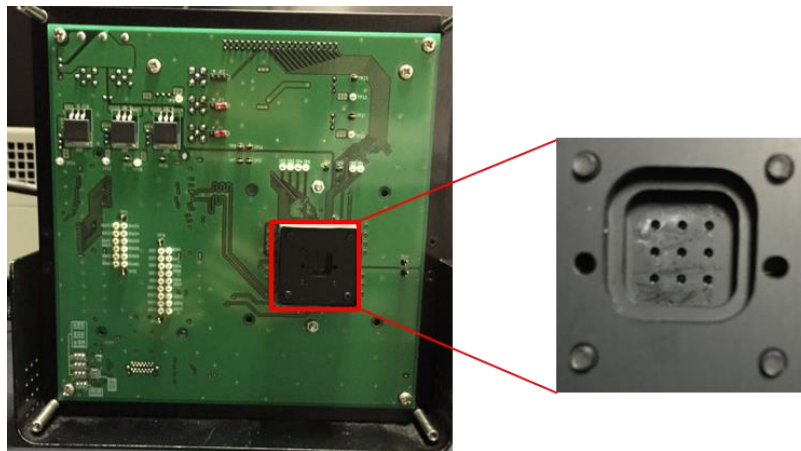


Figure 4. 1 Multi-aperture camera.

Figure 4. 1 shows the developed prototype multi-aperture camera. In this multi-aperture camera, a lens array is put on a single CMOS image sensor to emulate a multi-aperture system. The distance between each adjacent lens is 2mm both vertically and horizontally. The focal length and F-number of unit aperture is 3mm and 3.0, respectively. The synthetic F-number of the multi-aperture camera is 1.0.

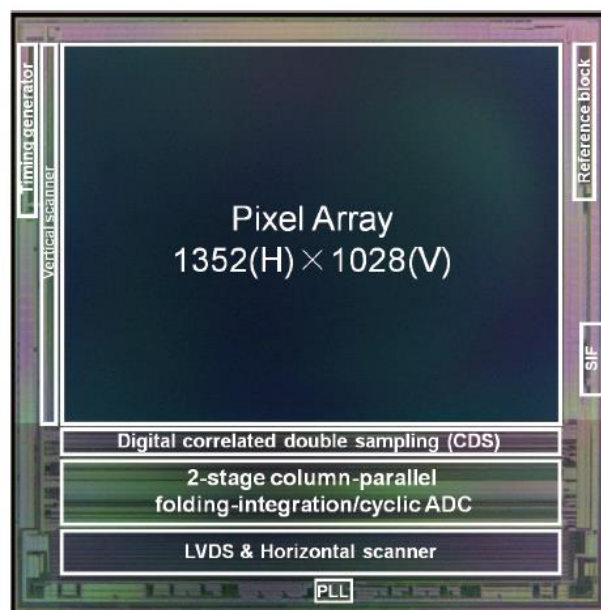


Figure 4. 2 Chip micrograph [9].

The micrograph of the CMOS image sensor used in the multi-aperture camera is shown in Figure 4. 2. This chip is fabricated in 1-poly 4-metal standard pinned photodiode 0.18 μm CMOS technology. The sensor noise can be reduced to $1.37e^-$ by the column parallel folding-integration and cyclic ADC. The DR can be extended to 85dB at 32 times sampling [1].

Table 4. 1 shows the summarized performance of high-performance sensor. The effective pixel number of this sensor is 1028(H) × 1284(V). However, in the multi-aperture camera, due to the sensor area is divided by the 3 × 3 lens array, the resolution of final reproduced image is reduced to 200 × 200.

Table 4. 1 Performance summary of applied CIS.

Parameter	Value
Technology	0.18 μm 1P4M CIS
Total area	10.0mm (H) × 13.5mm (V)
Power supplies	1.8 V (D), 3.3 V (A, D)
Number of pixels	1028 (H) × 1284 (V)
Pixel type	4 Tr. (Pinned photodiode)
Pixel size	7.1 μm × 7.1 μm
Fill factor	45%
ADC resolution	17b (Max.)
Input referred noise	$1.37e^-$ (Sampling = 32, $\Delta V_R = 2.0\text{ V}$)
Conversion gain	$82\mu\text{V}/e^-$
Full well capacity	$29,000e^-$
Dynamic range	85 dB (Sampling = 32, $\Delta V_R = 2.0\text{ V}$)

4.3 Image Reproduction Procedure

In this prototype multi-aperture camera, a standardization is operated to compensate the difference in intrinsic parameters among all apertures. The parallax caused by the extrinsic parameters was corrected by shifting the image manually in each aperture.

4.3.1 Standardization

The standardization is composed of the following steps.

- Undistortion
- Resizing
- Cropping

Undistortion

Lens distortion causes a major geometric disorder on image. In the image reproduction, because the selected apertures are averaged, the images of the apertures have to be completely consistent. As the first step for this purpose, images are undistorted with the extracted distortion parameters.

Resizing

In the multi-aperture camera, the focal length in each aperture has a slight difference to the other. There are many causes of the difference, such as manufacturing, assembling, and so on. As shown in Figure 4. 3(a), the longer the focal length is, the larger the image becomes. In the multi-aperture system, one aperture is chosen as the reference, and the images of the other apertures are resized to fit the reference image. The resize scale is defined as the ratio of focal length (f_i) to the reference focal length (f_0):

$$Scale_i = \frac{f_i}{f_0} \quad 4. 1$$

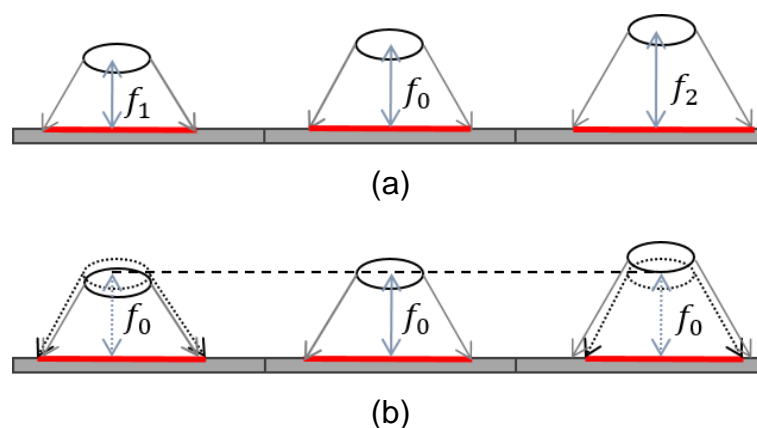


Figure 4. 3 Image resizing. (a) Different focal lengths and (b) resizing.

Cropping

Cropping is performed to compensate the differences of principal point and disparities among the apertures. The principle point is the position of image center, and disparity is measured based on it. Image area with the same size is cropped for every aperture, where the principal points or those plus disparities should be identical. The cropped images from the multi-aperture image become identical after standardization. Those images are used to reproduce a unified image by selective averaging.

Table 4. 2 The peak of noise histogram in each method (dark condition).

Method	Peak noise w/ standardization [e-]	Peak noise w/o standardization [e-]
Selective Averaging	0.30	0.48
Simple Averaging	0.30	0.48
Minimum Selection	0.68	1.16
Median Selection	0.40	0.70
Raw	0.81	1.38
Single Aperture Counterpart	0.09	0.16

In the standardization, interpolation that is weighted averaging of pixel values among the adjacent pixels is used. Therefore, the noise is reduced

apparently after interpolation, instead the spatial resolution is degraded a little. Table 4. 2 shows the peak of noise histogram in each method with and without standardization. The noise becomes smaller after standardization. In standardization, erroneous pixel values will spread to their adjacent pixels. However, such pixel values will be automatically removed by the selective averaging, which is because the image of the variance is also interpolated in the same way as normal images in aperture selection. The amount of the effective noise of pixel in the reproduced image is considered even when interpolation is applied.

4.3.2 Image Procedure

Figure 4. 4 shows the processing flow to reproduce a single image in the multi-aperture camera. In the preparation step, n-frame dark images are captured. Then, they are standardized with the above processing.

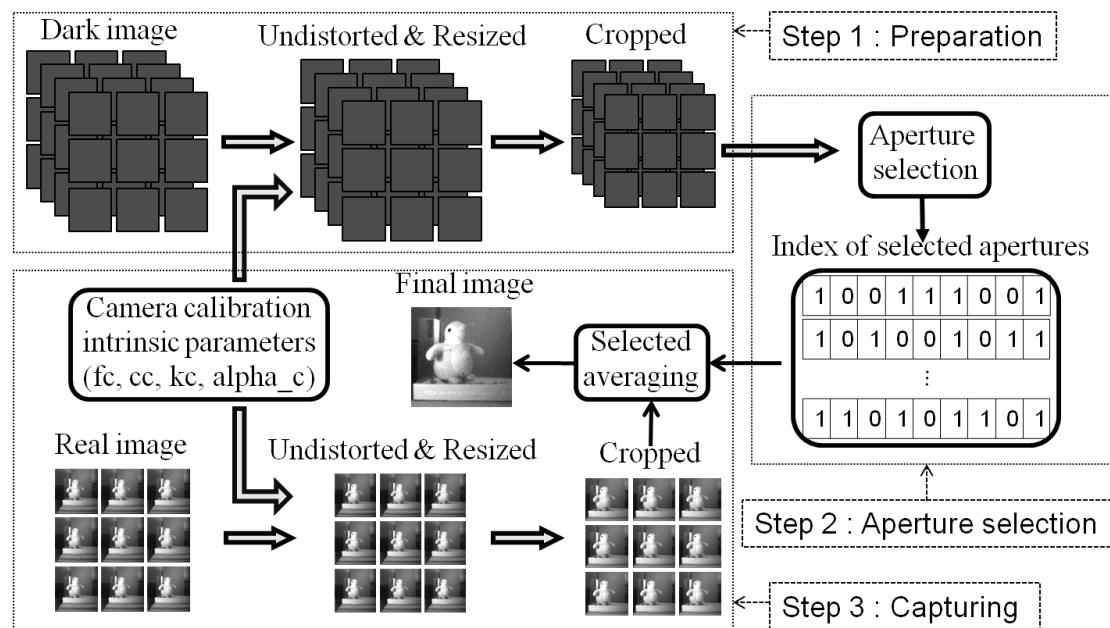


Figure 4. 4 Flow chart of single image reproduction.

In the aperture selection step, the standardized images are used to determine the selected apertures for every pixel by the selective averaging method. Indices “1” and “0” mean that the aperture is selected and is not selected, respectively. One row of the index table corresponds to one pixel

in the reproduced image, and it has nine binary digits for the nine apertures.

In the capturing step, the same standardization is operated to obtain the same-sized registered images for every aperture. Using the index table, which is calculated in the preparation step, selective averaging is applied pixel by pixel to reproduce the final image.

The preparation step is operated once after constructing the camera or image capturing because the variance of pixel noise in a dark condition and the camera parameters do not change in a short term as long as working environment is the same. However, the aperture selection step should be operated when the distance of subject changes. Because disparity is dependent on a subject distance, which means the index table has to be recalculated when the distance changes. Although, the sensor noise does not significantly change at around the room temperature, dark currents are very susceptible to temperature. Therefore, the noise variance changes due to the change in dark current shot noise. This issue can be solved with preparing several noise images for different temperatures or with thermal stabilization of the image sensors.

4.4 Experiment Results

In the experiments, the cropped area is adjusted to obtain a sharp reproduced image. This procedure can be automated based on an image matching technique. Figure 4. 5 shows the reproduced images for several methods and a synthetic reference image when the camera works under a low-light condition. The image of selective averaging shows the highest quality compared with those of the other methods. The reference image is synthesized by averaging 1,000 frames of one aperture image (the raw image) which are captured at 10°C, in that condition the dark current is significantly reduced. Due to the photon shot noise is very large in a bright environment, the dominant noise in the CIS is the photon shot noise. However, in a low-light condition, RTS noise or dark current becomes dominant. The illumination on the subject is 0.04, and the maximum average signal is around $11e^-$.

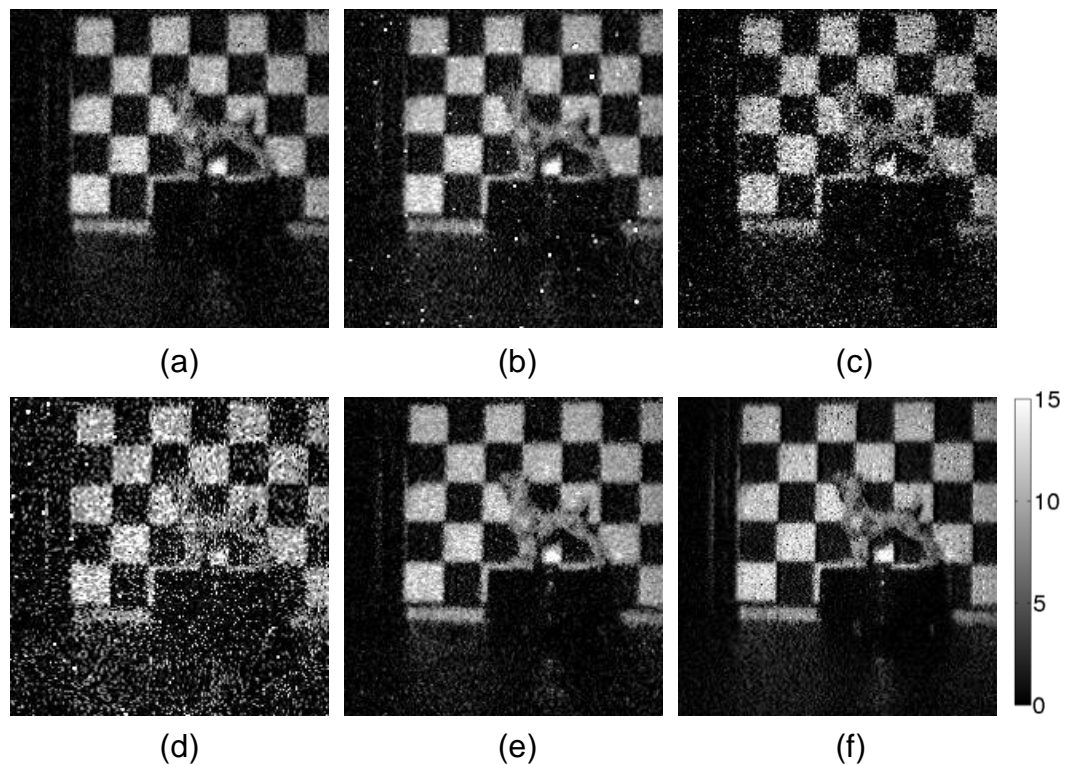


Figure 4. 5 Reproduced images and reference image. (a) Selective averaging, (b) simple averaging, (c) minimum selection, (d) median selection, (e) raw, and (f) reference.

Table 4. 3 shows the peak signal-to-noise ratio (PSNR) of the images in different methods and raw image when compared with the reference image. The selective averaging shows the largest PSNR value, and its improvement based on the raw image is 6.3dB. Because the simple averaging method cannot remove the large RTS noise and dark current, the PSNR of the simple averaging image is smaller than that of the selective averaging.

Table 4. 3 PSNR of the image for each method and raw.

Method	Selective Averaging	Simple Averaging	Minimum Selection	Median Selection	Raw
PSNR [dB]	18.70	18.02	14.59	18.57	12.41

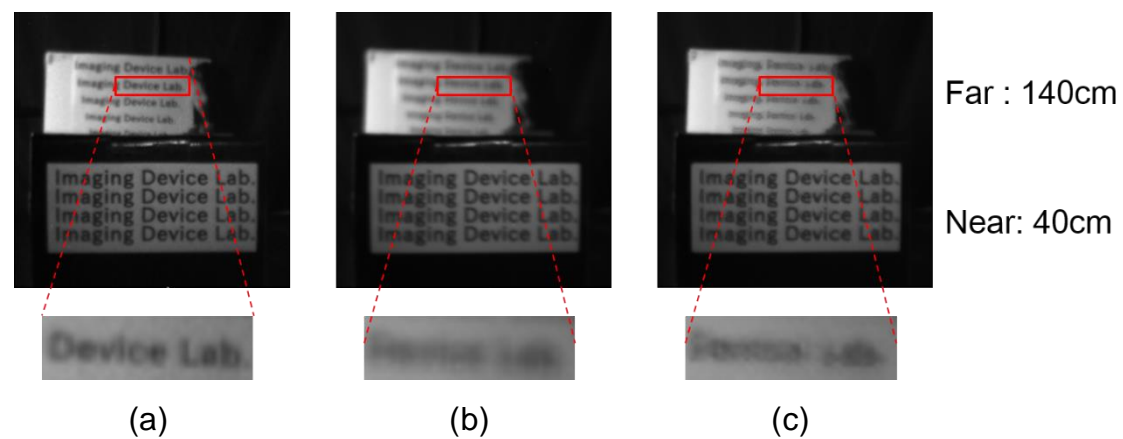


Figure 4. 6 Comparison of (a) Raw and virtually defocused image, (b) selective averaging, and (c) median selection.

Although the results for selective averaging and median selection give almost the same PSNR, selective averaging is preferable in terms of natural defocus emulation. As the multi-aperture system has disparity on the multi-aperture image, reproduced images become blurry when the real and a reproduction distance are different, which is called virtual defocus here. The defocus images of selective averaging, median selection, and raw are shown in Figure 4. 6, where the object distance of the near letters is 40 cm, and that of the far letters is 140 cm. If the median selection method is applied in the multi-aperture system, artifacts are generated in the virtually defocused

regions, because median selection does not have an averaging effect. While in the selective averaging method, the reproduced image becomes naturally blurred in the virtually defocused regions due to its averaging effect.

The numbers and percentages of the selected apertures are shown in Table 4. 4. The average number of the selected pixels is 8.35, which means the S/N of the reproduced image is significantly improved by the averaging effect. About 93% of the pixels are utilized in reproduction. As shown in Table 4. 4, more than half of the pixels select all apertures. The number of selected pixels correlates to the amount of sensor noise. If the noise histogram has a longer tail in a finer technology, the number of selected apertures will become smaller.

Table 4. 4 The numbers and percentages of the selected apertures.

Number of selected apertures	Number of pixels	Percentage [%]
1~4	0	0
5	30	0.1
6	688	1.7
7	4,663	11.7
8	14,405	36.0
9	20,214	50.5

4.5 Conclusion

In this chapter, a prototype multi-aperture camera which is composed of a low-noise high-sensitivity CMOS image sensor based on folding integration and cyclic ADC and a 3×3 lens array is described. In the experiment, a 3×3 -aperture camera, where each aperture has 200×200 pixels and an imaging lens with a focal length of 3.0 mm and F-number of 3.0, is utilized. In a low-light condition, in which the maximum average signal is $11e^-$ per aperture, the RTS noise and dark current white defects are removed and the peak signal-to-noise ratio (PSNR) of the image is increased by 6.3 dB.

Bibliography

- [1]. M. W. Seo, T. Sawamoto, T. Akahori, Z. Liu, T. Takasawa, T. Kosugi, T. Watanabe, K. Isobe, and S. Kawahito, "A low-noise high-dynamic range 17-b 1.3-Mpixel 30-fps CMOS image sensor with column-parallel two-stage folding-integration cyclic ADC," IEEE Transactions on Electron Devices, vol. 59, no. 12, pp.3396-3400, Dec. 2012.
- [2]. M. W. Seo, T. Sawamoto, T. Akahori, T. Iida, T. Takasawa, K. Yasytomi, and S. Kawahito, "A low noise wide dynamic range CMOS image sensor with low-noise transistors and 17b column-parallel ADCs," IEEE Sensor Journal, vol. 13, no. 8, pp. 2922-2929, Aug. 2013.
- [3]. C. Lotto, P. Seitz, and T. Baechler, "A sub-electron readout noise CMOS image sensor with pixel-level open-loop voltage amplification," IEEE International Solid-State Circuits Conference, pp. 120-404, Feb. 2011.
- [4]. S. F. Yeh, K. Y. Chou, H. Y. Tu, C. Y. P. Chao, and F. L. Hsueh, "A 0.66e-rms temporal-readout-noise 3D-stacked CMOS image sensor with conditional correlated multiple sampling (CCMS) technique," in Symp. VLSI Circuits Digest of Technical papers, pp. C84–C85, Jun. 2015.
- [5]. S. Wakashima, F. Kusuhara, R. Kuroda, and S. Sugawa, "A linear response single exposure CMOS image sensor with 0.5e- readout

- noise and 76ke- full well capacity,” in Symp. VLSI Circuits Digest of Technical papers, pp. C88–C89, Jun. 2015.
- [6]. C. Leyris, F. Martine, M. Valenza, A. Hoffmann, J. C. Vildeuil, and F. Roy, “Impact of random telegraph signal in CMOS image sensor for low-light levels,” 32nd European Solid-State Circuits Conference, pp. 376-379, Sep. 2006.
- [7]. X. Y. Wang, P. R. Rao, A. Mierop, and A. J. P. Theuwissen, “Random telegraph signal in CMOS image sensor pixels,” International Electron Devices Meeting, pp. 1-4, Dec. 2006.
- [8]. P. Martin-Gonthier, and P. magnan, “RTS noise impact in CMOS image sensors readout circuit,” 16th International Conference on Electronics, Circuits, and System, pp. 928-931, Dec. 2009.
- [9]. Min-Woong Seo, “A Study on Low-Noise High Dynamic Range High Resolution CMOS Image Sensors with Folding-Integration/Cyclic ADCs,” Doctoral Thesis, Shizuoka University, 2012.
- [10]. B. Zhang, K. Kagawa, T. Takasawa, M. W. Seo, K. Yasutomi, and S. kawahito, “RTS noise and dark current white defects reduction using selective averaging based on a multi-aperture system,” Sensors, vol. 14, pp. 1528-1534, Jan. 2014.

Chapter 5

Low-Noise Performance

Demonstration by 2×2 -Aperture

Color Camera

5.1 Introduction

A low-light multi-aperture monochrome camera, which is suitable for capturing movies and is much more compact than single-lens cameras with the same F-number, based on multi-aperture optics and a selective averaging is proposed [1]. In the multi-aperture camera, a reproduced image is synthesized by averaging the images from each aperture to enhance the image quality. However, large random noise components of the CMOS image sensor cannot be eliminated by simple averaging. To remove these kinds of noise, the selective averaging is proposed. This method is based on a one-pass algorithm and does not need any iteration. Therefore, it is possible to apply this method to real-time movie acquisition. The effectiveness of the selective averaging has verified by experiments in a prototype 3×3 -aperture monochrome camera which was introduced in Chapter 4.

Compared with monochrome camera, in the color camera, interpolation is needed, which will increase the size of bright spots. Thus, the noise of low-light image in the color camera is more visible than that in the monochrome

camera at the same exposure. To demonstrate the performance of selective averaging in color, a 2×2 -aperture color camera is developed [2].

In this chapter, the effectiveness of the selective averaging for color imaging has been verified qualitatively by simulation. The color reproduction error after the selective averaging is quantitatively evaluated in the CIE-xy 1931 color space.

5.2 Multi-Aperture Color Camera & Image Procedure

5.2.1 2×2 Multi-Aperture Color Camera

The photograph of 2×2 multi-aperture color camera is shown in Figure 5. 1. The multi-aperture camera is composed of 2×2 sets of a low-noise and high-dynamic-range CMOS image sensor and a bright video lens with an F-number of 1.2 and a focal length of 8mm. The synthetic F-number becomes 0.6. This CMOS image sensor is composed of $1280 (H) \times 1024 (V)$ effective pixels whose pitch is $7.1\mu\text{m} \times 7.1\mu\text{m}$. It has the same pixel structure and column readout circuits as Reference [3] except being equipped with Bayer color-filters. The pitch of the apertures is $110\text{mm} \times 110\text{mm}$. Because the size of the print circuit board (PCB) is $220\text{mm} \times 220\text{mm}$, the scale of the aperture array is extensible by tiling the PCBs with keeping the aperture pitch all the same. This PCB has two channels of CameraLink, and transfers the captured images at the maximum frame rate of 30 frame per second (fps).

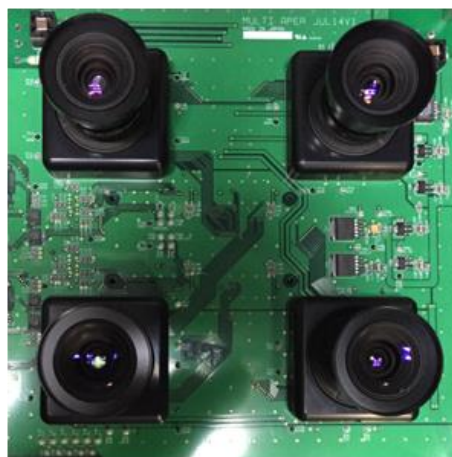


Figure 5. 1 Photograph of 2×2 multi-aperture color camera.

5.2.2 Image Procedure

Figure 5. 2 shows the flow chart of color image reproduction for Bayer color-filter image sensors. Although the operation is basically the same as that for monochrome image sensors which is shown in Section 4.3, interpolation to deal with sparse spatial sampling by the color filters is added.

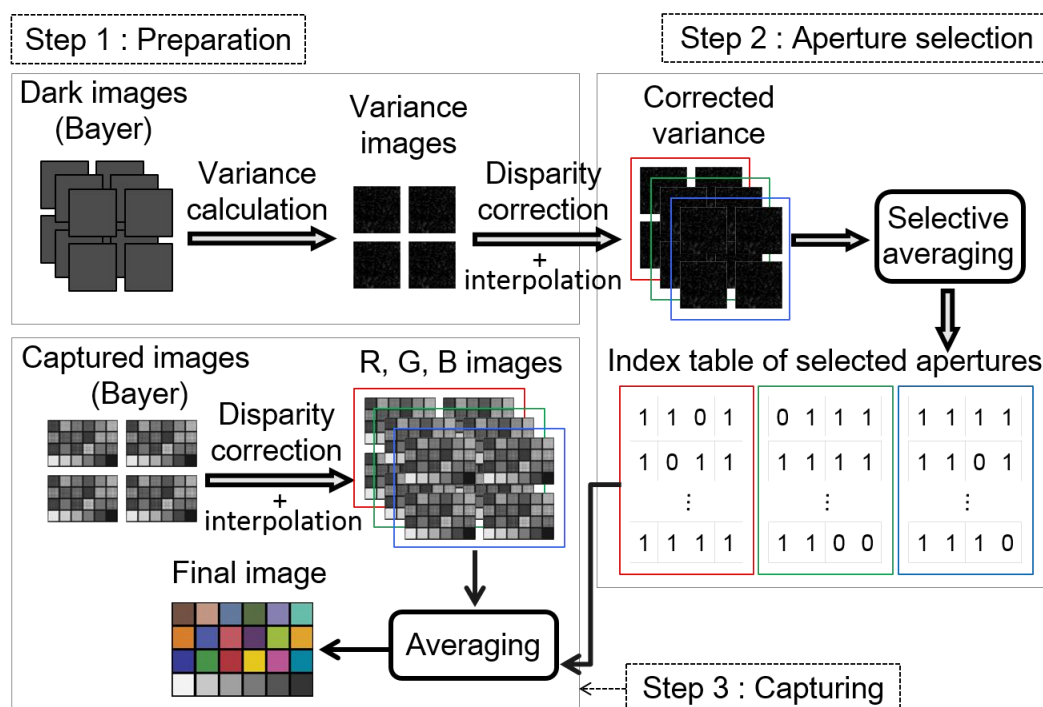


Figure 5. 2 Image reproduction flow char.

Image acquisition is composed of two steps: aperture selection and capturing. Because the multi-aperture camera has parallax, it is necessary to eliminate it by disparity correction based on the intrinsic and extrinsic camera parameters, and the distance of subject. The disparity correction is performed only when the subject distance or a camera parameter such as the focal length for zooming changes. The details of this procedure are described in Appendix. The same disparity correction is performed on the dark variance images for apertures selection as well as the captured images. Because Bayer color-filters are assumed in this paper, both of the variance and the captured images for R, G, and B channels are sparse. After the disparity correction, dense images are generated by interpolation. In the aperture selection, the selective averaging is applied to determine the selected aperture for R, G, and B channels separately, so that an index table showing the selected apertures is obtained.

In capturing, M images captured at the same time are selectively averaged after the disparity correction in R, G, and B channels respectively to reproduce a single noise reduction image based on the indices table of the selected apertures.

5.3 Results

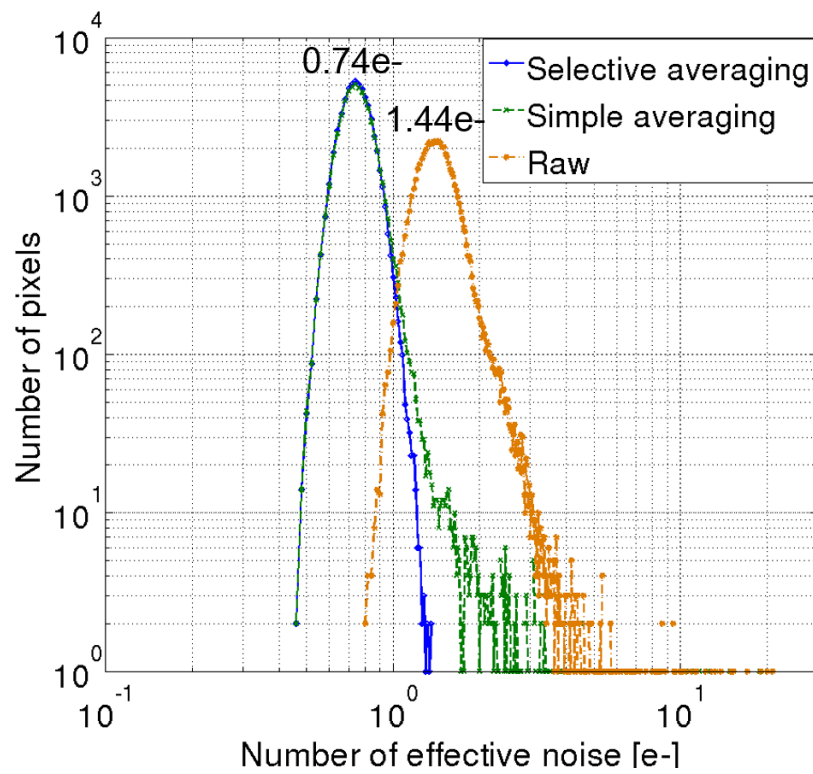


Figure 5. 3 Noise distribution.

The noise distribution in dark of the 2×2 multi-aperture camera is shown in Figure 5. 3. In this simulation, real measured noise of the CMOS image sensor applied in the 3×3 -aperture monochrome camera which was discussed in Chapter 4 is used. Again, the "Raw" shows the measured sensor noise itself. The histograms of simple averaging and selective averaging are also shown in the figure. The noise of the simple averaging is reduced to approximately a half of the raw in the peak of noise histogram. However, the large noise components in the tail of the histogram remain. On the other hand, they are removed with the selective averaging. Compare with noise distribution of the 3×3 -aperture monochrome camera in selective averaging, the noise is increased because the number of apertures are decreased.

Reproducibility of color is verified with the noise model shown in Figure 5. 4. A hand-made color-checker image imitating the Macbeth color checker is

used in simulation. The pixel count is 300×200 . Firstly, a Bayer color-filter image, which is basically a single-layer monochromatic image, is generated from the RGB-color color-checker image. To simulate a low-light condition, the maximum pixel value of the captured image is set to as small as 10 electrons. Measured sensor noise and simulated photon shot noise are added to obtain a noisy image. No disparity is considered in this simulation.

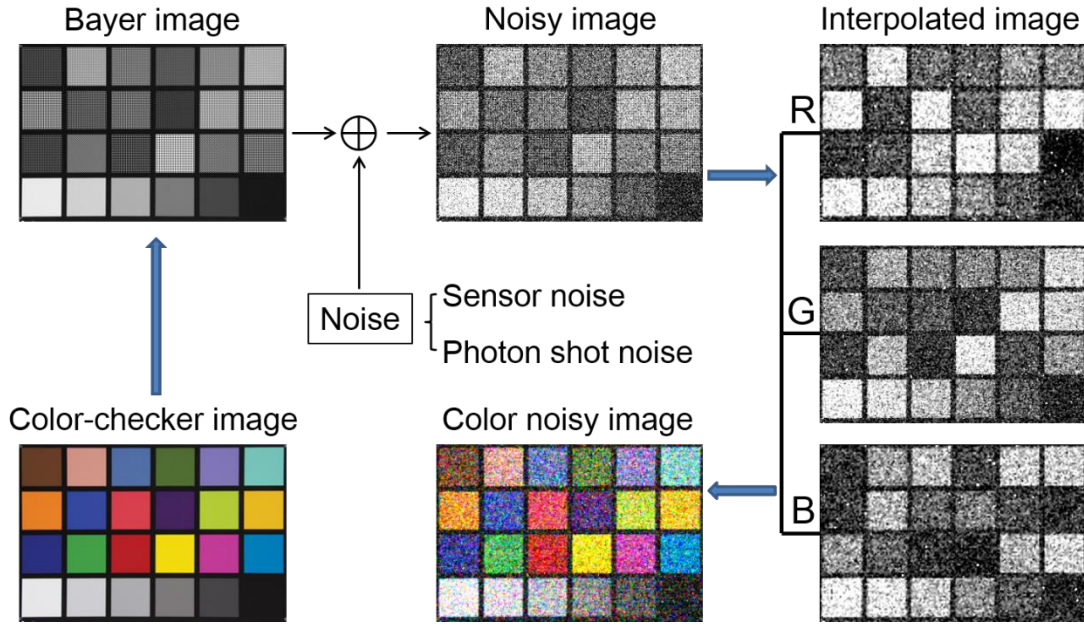


Figure 5. 4 Noise simulation model.

Figure 5. 5(a)-(c) show the reproduced images of selective averaging, simple averaging, and raw, respectively. Figure 5. 5(d) shows the original image. For the raw image, granular structure caused by interpolation is observed. Because the photon shot noise is large, RTS noise and dark current shot noise are not visible in the bright regions. For the simple averaging, bright noise spots are observed because the pixels with large noise are included in averaging. Each of Figure 5. 5(a)-(c) is accompanied by enlarged images for G, B, and grey regions from the top to the bottom, respectively. As shown in the enlarged image of Figure 5. 5(b), there are several bright dots with different colors from the original color, which look like primary colors, namely, R, G, or B. It is because the probability that more than one pixel has large noise is very small; only one component among R,

G, and B channels has large noise. For the selective averaging, granularity seen in Figure 5. 5(c) becomes smaller by virtue of averaging. In addition, large noise pixels are removed. Thus, the quality of the reproduced image is improved significantly with the selective averaging.

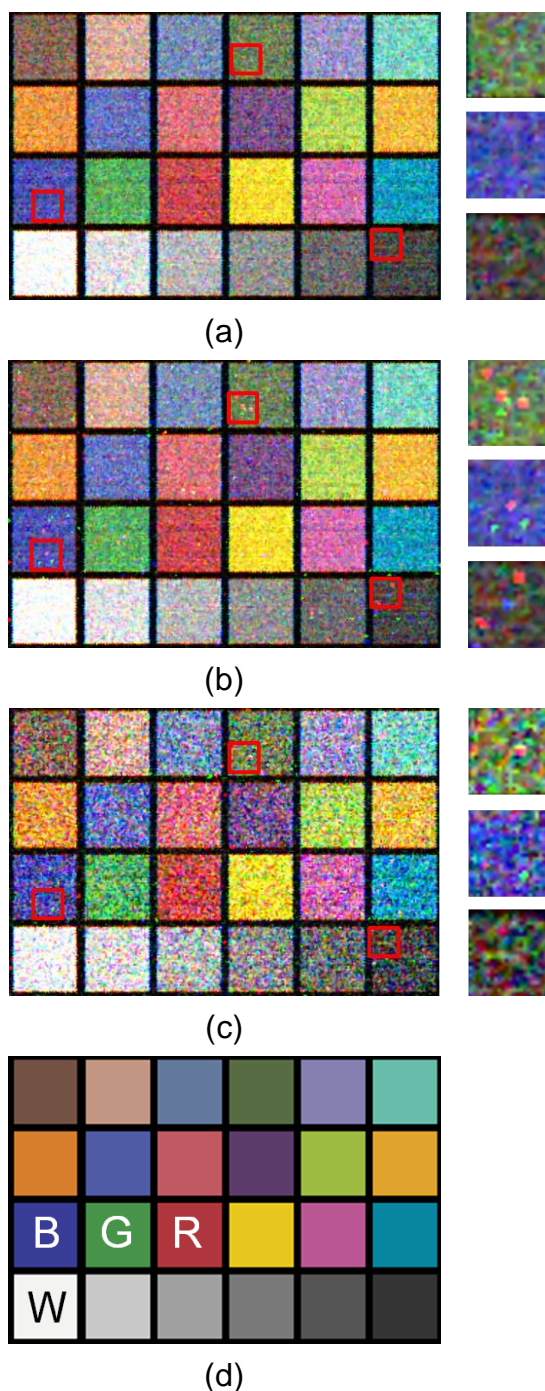


Figure 5. 5 Reproduced images for (a) selective averaging, (b) simple averaging, (c) raw, and (d) original.

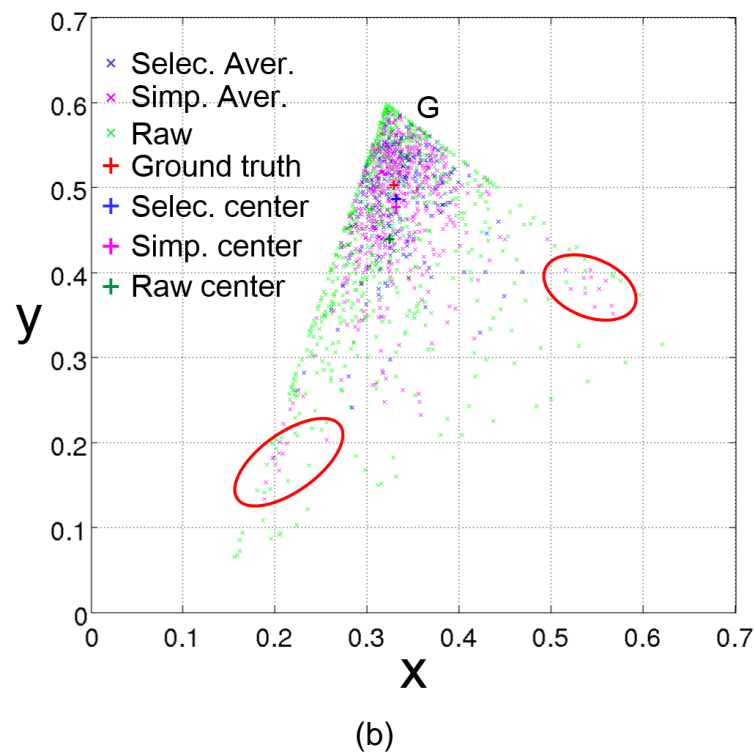
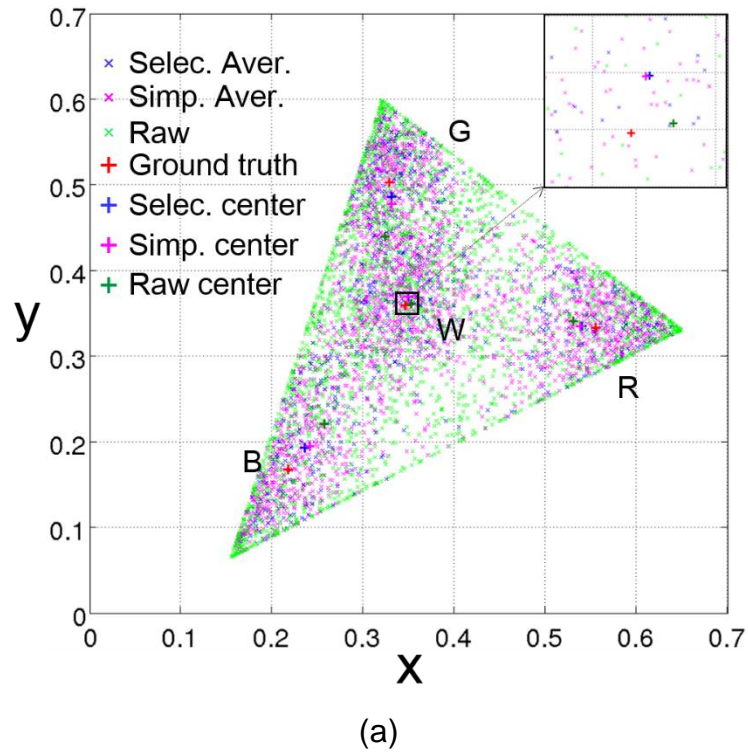


Figure 5. 6 Distributions for selective averaging, simple averaging, and raw in CIE-xy color space: (a) R, G, B, and W colors and (b) G only. (Selec.: selective, Simp.: simple, Aver.: averaging)

Figure 5. 6 shows the effectiveness of the noise reduction methods in the CIE-xy 1931 color space, where the selective averaging, the simple

averaging and the raw are compared. In Figure 5. 6(a), the distributions of the reproduced color coordinates for the R, G, B, and W areas are shown. The ground truth indicates a true color coordinate in the original color-checker image, which is shown as a point. Figure 5. 6(a) shows that the distributions for the selective averaging and the simple averaging are smaller than that of the raw image. In Figure 5. 6(b), the distribution only for the G area is indicated to clearly show the effectiveness of the selective averaging. The distributions of the selective averaging and the simple averaging are smaller than that of the raw, which means the noise is reduced. The data points of the simple averaging in the circles that are located in the areas of B and R correspond to large noise shown in Figure 5. 5(b). Thus, the distribution of the selective averaging is the smallest.

Table 5. 1 Color reproduction errors in CIE-xy color space.

		Selective Averaging	Simple Averaging	Raw
B (x, y)=(0.2176, 0.1676)	σ	0.0875	0.0969	0.1569
	Distance	0.0313	0.0361	0.0666
G (x, y)=(0.3286, 0.5027)	σ	0.0729	0.0910	0.1370
	Distance	0.0167	0.0258	0.0636
R (x, y)=(0.5552, 0.3331)	σ	0.0722	0.0757	0.1259
	Distance	0.0151	0.0164	0.0257
W (x, y)=(0.3463, 0.3594)	σ	0.0611	0.0617	0.1028
	Distance	0.0105	0.0103	0.0070

Table 5. 1 shows the calculated errors in terms of standard deviation σ and distance between the gravity center of the distribution and the point of the ground truth. The standard deviation and distance of the selective averaging is smaller than that of the simple averaging, which are approximately a half as much as that of the raw. This result is reasonable because at most four pixel values are averaged.

5.4 Conclusion

In this chapter, a color image reproduction method based on a multi-aperture camera and selective averaging for low-noise movie capturing is proposed. This method eliminates extremely large noise such as RTS noise and dark current shot noise, and increases the signal to noise ratio. For a 2×2 -aperture camera using Bayer color-filter low-noise CMOS image sensors, simulation results show that the effective noise in terms of the peak of noise in histogram is reduced from $1.44e^-$ to $0.74e^-$, and RTS noise and large dark current shot noise are successfully removed. Color reproduction errors are quantitatively evaluated. The root-mean-square errors of blue, green, and red in the CIE-xy 1931 color space becomes approximately a half after the selective averaging.

Because the multiple images cannot be acquired simultaneously by the 2×2 -aperture color camera so far, in this chapter, the color performance in low-light conditions is only demonstrated by simulation. In the near future, we will work on real image capturing and real-time processing by selective averaging.

To further enhance the low-light performance by multi-aperture camera, the number of aperture can be increased. However, the size of camera body will increase with the aperture number increasing. The performance can also be enhanced by sensor noise reduction. A low-noise CMOS image sensor, where the read noise in the peak of noise histogram has been reduced to $0.27e^-$ by high conversion gain, is designed [4]. In the future, a low-noise high-sensitivity multi-aperture camera will be fabricated based on this high conversion gain image sensor to enhance the low-light performance.

Bibliography

- [1]. B. Zhang, K. Kagawa, T. Takasawa, M. W. Seo, K. Yasutomi, and S. Kawahito, "RTS noise and dark current white defects reduction using selective averaging based on a multi-aperture system," *Sensors*, vol. 14, pp. 1528-1534, Jan. 2014.
- [2]. B. Zhang, K. Kagawa, T. Takasawa, M. W. Seo, K. Yasutomi, and S. Kawahito, "Low-light color reproduction by selective averaging in multi-aperture camera with Bayer color filter low noise CMOS image sensors," *ITE Transactions on Media Technology and Applications*, vol. 3, no. 4, pp. 234-239, Jun. 2015.
- [3]. M. W. Seo, T. Sawamoto, T. Akahori, Z. Liu, T. Takasawa, T. Kosugi, T. Watanabe, K. Isobe, and S. Kawahito, "A low-noise high-dynamic range 17-b 1.3-Mpixel 30-fps CMOS image sensor with column-parallel two-stage folding-integration cyclic ADC," *IEEE Transactions on Electron. Device*, vol. 59, no. 12, pp.396-3400, Dec. 2012.
- [4]. M. W. Seo, S. Kawahito, K. Kagawa, and K. Yasutomi, "A $0.27 e_{\text{rms}}^-$ read noise $220 \mu\text{V}/e^-$ conversion gain reset gate less CMOS image sensor with $0.11 \mu\text{m}$ CIS process," *IEEE Electron Device Letters*, vol. 36, no. 12, pp. 1344-1347, Dec. 2015.

Chapter 6

Conclusion

The noise in recent CMOS image sensors has greatly reduced, which makes it possible to apply them to low-light applications. Compared with CCD, however, there are some large noise components in CMOS image sensor, which greatly degraded the low-light image quality.

To enhance the low-light image quality, in this study, a multi-aperture imaging system which consists of lens and CMOS image sensor array for increasing optical gain and selective averaging for removing extraordinary large noise components of CMOS image sensor in the reproduced image, is proposed.

Chapter 3 presents a structure of multi-aperture imaging system. In the multi-aperture imaging system, a synthetic F-number which is smaller than the F-number of unit lens can be achieved and defect pixel interpolation is not necessary. The SNR of multi-aperture imaging system is analyzed by comparing with that of single aperture counterpart. The SNR of multi-aperture imaging system is degraded due to amplified sensor noise. However, the degradation can be decreased by reducing sensor noise. When the sensor noise is reduced below $0.3e^-$, the degradation can be ignored. The simultaneously acquired multiple images are noisy due to poor SNR in low-light conditions. Averaging is an available method to increase the SNR. But the performance is limited by the large noise component which is composed of RTS noise and dark current shot noise. A selective averaging

is proposed to exclude those kinds of large noise before averaging. This method is operated pixel by pixel. A pixel in a reproduced image has multiple sub-pixels. The pixel value of the reproduced image is calculated by averaging the pixel values of the selected sub-pixels only. The selected sub-pixels are determined by a minimized combination variance which is calculated by the variance of pixel value of the correlated sub-pixels in the dark condition. Large noise causes large variance. If the variance is relatively large, a larger combination variance is brought. Thus, the sub-pixels with large noise are automatically excluded by selective averaging. In the simulation, the effective dark sensor noise is reduced from $1.38e^{-}$ to $0.48e^{-}$ in the peak of noise histogram.

Chapter 4 introduces a prototype multi-aperture camera which is composed of a compact 3×3 lens array and a low-noise CMOS image sensor based on the folding integration and cyclic column ADC. This sensor which is fabricated in $0.18\mu\text{m}$ CMOS technology has the effective pixel of $1284\text{ (H)} \times 1028\text{ (V)}$. However, the sensor is divided by the lens array to emulate multi-aperture imaging system, and the pixel count of reproduced image is 200×200 . In the image reproduction procedure, a standardization which consists of un-distortion, resizing and cropping, is operated on preparation and capturing to ensure a uniformity in simultaneously acquired images. The selective averaging is compared with simple averaging, minimum selection, median selection, raw, and the single aperture counterpart to verify its effectiveness. In the experiment, the peak signal-to-noise ratio (PSNR) of the image is increased by 6.3dB when compared with the raw in a low-light condition where the illumination on the surface of test pattern is 0.04lx and the maximum average signal is $11e^{-}$. The RTS noise and dark current white defects are removed completely.

Chapter 5 introduces a prototype low-noise high-sensitivity 2×2 -aperture color camera. In each aperture, a bright lens which has the F-number of 1.2 and the focal length of 8mm and a Bayer color-filter based low-noise CMOS image sensor is utilized. Compared with previous work, the resolution of

reproduced image is increased. Moreover, the performance of selective averaging is demonstrated in color. In the color image procedure, all the processing is operated on R, G, and B channels, respectively. In the simulation, the effective noise in the peak of noise histogram is reduced from $1.44e^-$ to $0.74e^-$. RTS noise and large dark current shot noise are successfully removed. The color reproduction errors are quantitatively evaluated. The root-mean-square errors of B, G, and R in the CIE-xy color space becomes approximately a half after the selective averaging.

This study verifies the effectiveness of the multi-aperture imaging system with selective averaging in low-light applications. In the future, the transistor will scale down, and RTS noise will increase. While the noise level of CMOS image sensor will be reduced by high conversion gain in fine technology. The low-light performance of the multi-aperture imaging system with selective averaging will be further extended. However, if the sensor noise can be reduced to the photon counting level in the future, the noise in CMOS image sensor becomes quantization. In such a situation, the effectiveness of the selective averaging should be re-verified.

Appendix

Disparity Correction

In the multi-aperture imaging system, the pixel value of the reproduced image is calculated by averaging the pixel value of the selected apertures in each pixel. So before averaging, the simultaneously acquired images by the multi-aperture imaging system should be the same. However, the images are different each other due to parallax and the slight differences in the intrinsic parameters which include focal length (f), principal point (c), skew (α), distortion coefficient (K) and the extrinsic parameters, which include rotation (R) and translation (T). Thus, the images need to be corrected before the selective averaging.

In the ideal multi-aperture imaging system, as shown in Figure A. 1 (a), no lens distortion and rotation should be considered. The parallax can be easily calculated by:

$$\Delta x = -f \cdot \frac{X}{Z}, \Delta y = -f \cdot \frac{Y}{Z} \quad \text{A. 1}$$

In the real multi-aperture imaging system, however, due to the difference in intrinsic and extrinsic parameters among apertures, the parallax calculation becomes difficult. To correct the images, a disparity correction is used.

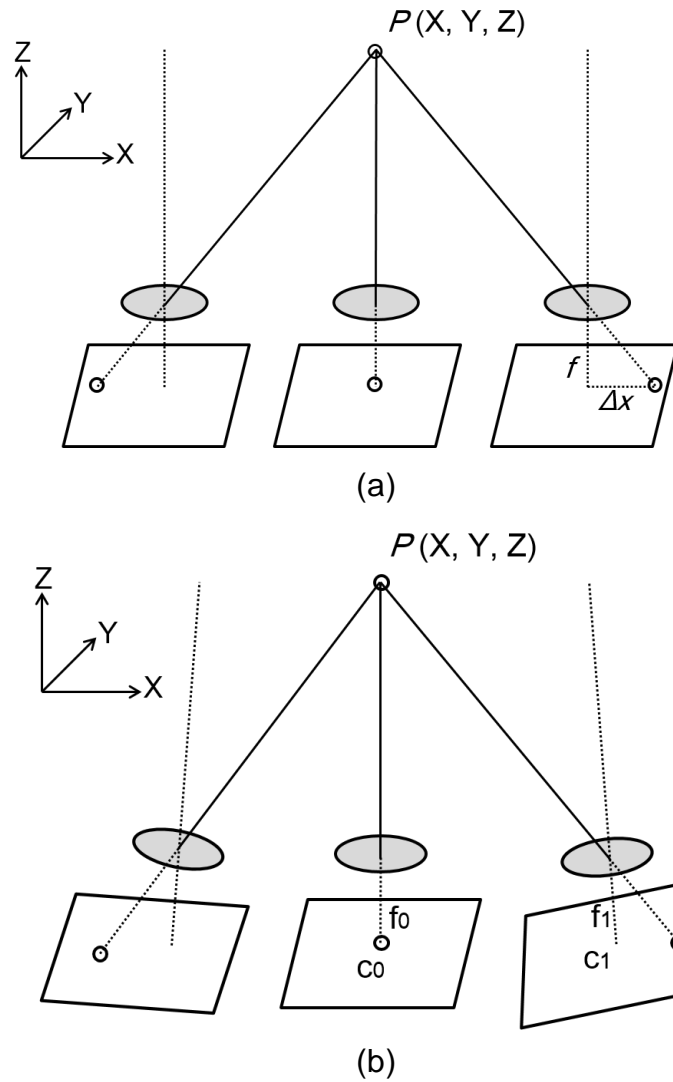


Figure A. 1 Camera model of (a) ideal and (b) real.

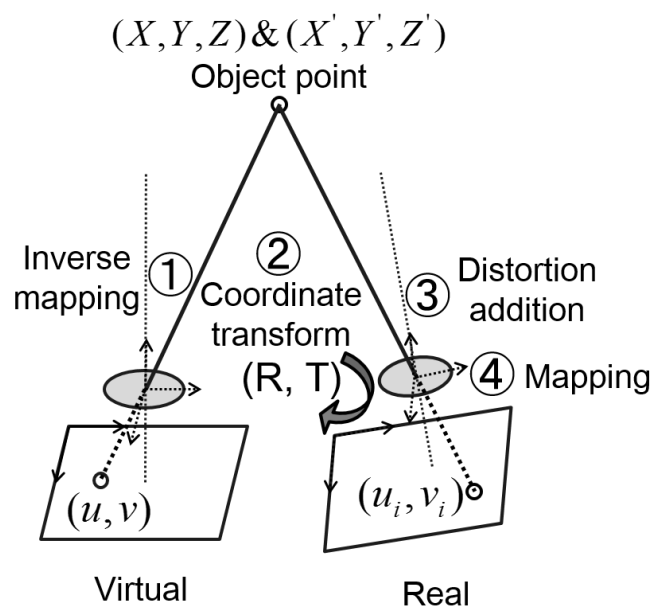


Figure A. 2 Schematic diagram of disparity correction.

Figure A. 2 shows the schematic diagram of the disparity correction. The virtual camera is assumed as an ideal camera which does not have any lens distortion. The coordinate of the object point (X, Y, Z) can be easily calculated under the pin hole model by using the pixel coordinate of the projective point (u, v) in the virtual camera. This operation is called inverse mapping. The calculated coordinate of object point is under the virtual camera coordinate system. It is transformed to the real camera coordinate system (X', Y', Z') by using the extrinsic parameters of the real camera. After coordinate transform, the lens distortion of the real camera is added to the coordinate of object point. Then, the distorted coordinate is mapped to the pixel coordinate (u_i, v_i) of the real camera. The equation of the operations are shown below:

$$\begin{bmatrix} X \\ Y \\ Z \end{bmatrix} = Z_v \cdot \begin{bmatrix} \frac{1}{f_{vx}} & 0 & -\frac{c_{vx}}{f_{vx}} \\ 0 & \frac{1}{f_{vy}} & -\frac{c_{vy}}{f_{vy}} \\ 0 & 0 & 1 \end{bmatrix} \begin{bmatrix} u - c_{vx} + 0.5 \\ v - c_{vy} + 0.5 \\ 1 \end{bmatrix} \quad \text{A. 2}$$

$$\begin{bmatrix} X'_i \\ Y'_i \\ Z'_i \end{bmatrix} = R_i \begin{bmatrix} X - T_{Xi} \\ Y - T_{Yi} \\ Z - T_{Zi} \end{bmatrix} \quad \text{A. 3}$$

$$x' = x(1 + k_1 r^2 + k_2 r^4 + k_3 r^6) + 2p_1 xy + p_2(r^2 + 2x^2)$$

$$y' = y(1 + k_1 r^2 + k_2 r^4 + k_3 r^6) + p_1(r^2 + 2y^2) + 2p_2 xy$$

$$(x = X'_i/Z'_i, \quad y = Y'_i/Z'_i, \quad r^2 = x^2 + y^2)$$

$$(K_i = [k_1, k_2, p_1, p_2, k_3]) \quad \text{A. 4}$$

$$u_i = f_{xi} \cdot (x' + \alpha_i y') + c_{xi}, \quad v_i = f_{yi} \cdot y' + c_{yi} \quad \text{A. 5}$$

The subscript vx and vy expresses the virtual camera parameters and subscript xi and yi expresses the real camera parameters. In the multi-

aperture camera, i also expresses the aperture number and it is in the range of 1 to M . The intrinsic and extrinsic parameters can be calculated by camera calibration. z_v is the only variable element. It defines the distance between the cameras to the object. If the distance z_v is given, the image disparity can be corrected automatically.

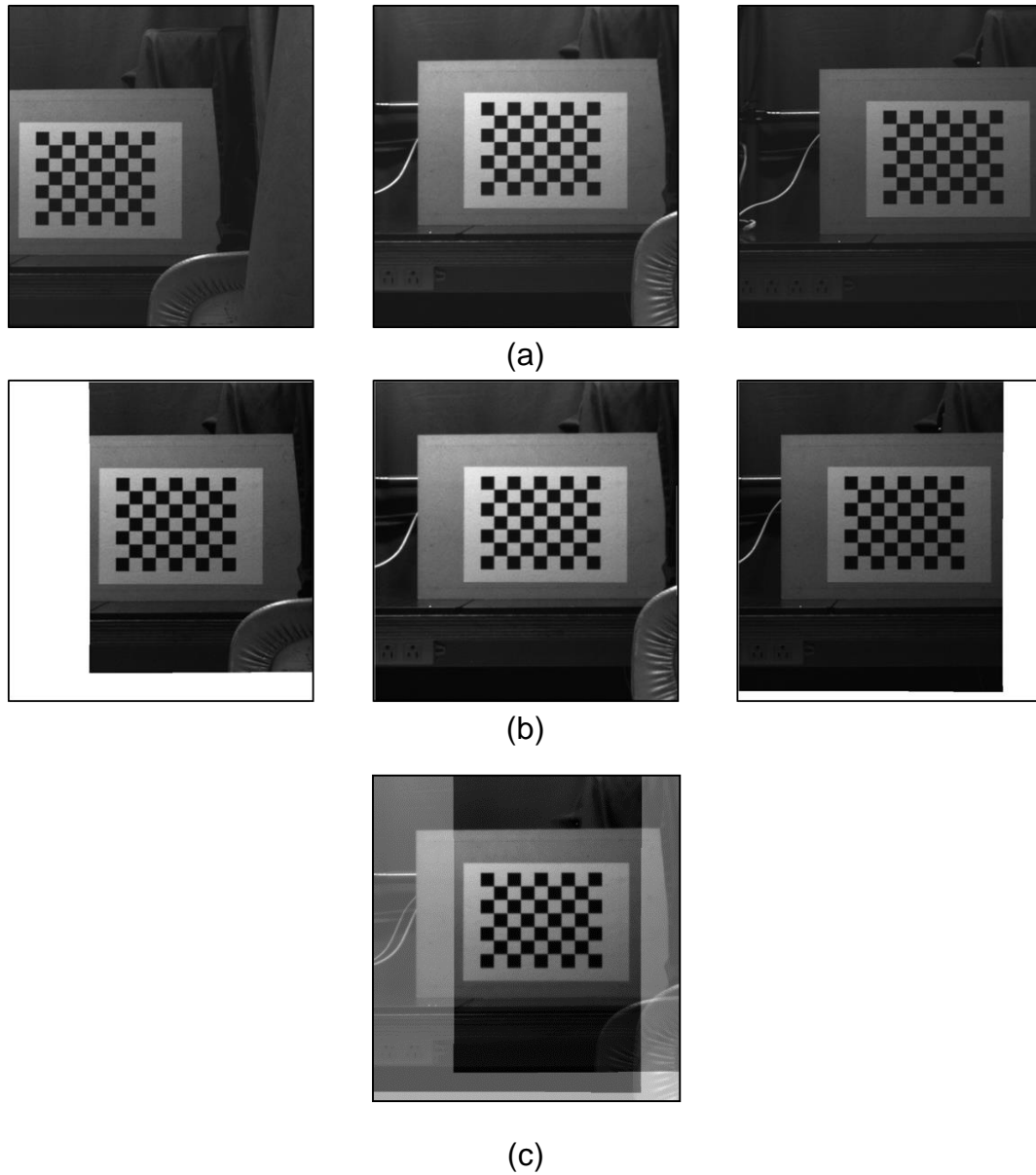


Figure A. 3 Disparity correction. (a) Captured images, (b) corrected images, and (c) image registration.

In the disparity correction operation, one aperture is selected as the reference. The focal length and the principal point of the virtual camera are selected as those of the reference camera. The extrinsic parameters of

reference camera are zero. The extrinsic parameters of the other apertures are calculated with respect to the reference camera respectively by stereo calibration. The calculated pixel coordinates (u_i, v_i) of the real cameras are different from ideal ones due to distortion. Therefore, interpolation is needed. After disparity correction and interpolation the image in all apertures become uniform.

Figure A. 3 shows the performance of the disparity correction. Here three cameras are used. They are placed in a line to capture a test pattern. The distance between two adjacent cameras is 10cm. The center camera is the reference camera. The captured images are shown in Figure A. 3 (a). Due to the parallax and different lens distortion, the position of the test pattern in each camera is different. The corrected images are shown in Figure A. 3 (b). The white part shows the region out of the source image. Figure A. 3 (c) shows the image after registration. The test pattern in all cameras is completely registered.

List of publications

Journal Papers

1. B. Zhang, K. Kagawa, T. Takasawa, M-W. Seo, K. Yasutomi, and S. Kawahito, "RTS Noise and Dark Current White Defects Reduction Using Selective Averaging Based on a Multi-Aperture System," MDPI Sensors, vol.14, no.1, pp.1528-1543, Jan. 2014.
2. B. Zhang, K. Kagawa, T. Takasawa, M-W. Seo, K. Yasutomi, and S. Kawahito, "Low-light color reproduction by selective averaging in multi-aperture camera with Bayer color filter low noise CMOS image sensors," ITE Transactions on Media Technology and Applications, vol. 3, no. 4, pp. 234-239, Jun. 2015.
3. F. Mochizuki, K. Kagawa, S-I. Okihara, M-W. Seo, B. Zhang, T. Takasawa, K. Yasutomi, and S. Kawahito, "Single-event transient imaging with an ultra-high-speed temporally compressive multi-aperture CMOS image sensor," OSA Optics Express, vol. 24, no. 4, pp. 4155-4176, Feb. 2016.
4. M. H. Conde, B. Zhang, K. Kagawa, and O. Loffeld, "Low-light image enhancement for multiaperture and multitap system," IEEE Photonics Journal, vol. 8, no. 2, Apr. 2016. (Accepted)

International Symposia

1. F. Mochizuki, K. Kagawa, S-I. Okihara, M-W. Seo, B. Zhang, T.

- Takasawa, K. Yasutomi, and S. Kawahito, "Single-Shot 200Mfps 5×3 -Aperture Compressive CMOS Imager," IEEE International Solid-State Circuits Conference, Digest of Technical Papers, 6.4, vol.58, pp.116-117, Feb. 2015.
2. B. Zhang, K. Kagawa, T. Takasawa, M-W. Seo, K. Yasutomi, and S. Kawahito, "A High-Sensitivity 2×2 Multi-Aperture Color Camera Based on Selective Averaging," Electric Imaging 2015, 9403-11, Feb. 2015.
 3. B. Zhang, K. Kagawa, T. Takasawa, M-W. Seo, K. Yasutomi, and S. Kawahito, "A High-Sensitivity 2×2 Multi-Aperture Color Camera Based on Selective Averaging," International Symposium toward the Future of Advanced Researches in Shizuoka University, PS-1, pp.41, Jan. 2015.
 4. P-S. Sivakumar, K. Kagawa, M-W. Seo, B. Zhang, T. Takasawa, K. Yasutomi, and S. Kawahito, "Measurement of 3-Tap 1MS/s CMOS Image Sensor for Multi-Point Fluorescence Correlation Spectroscopy," International Symposium toward the Future of Advanced Researches in Shizuoka University, PS-3, pp.43, Jan. 2015.
 5. K. Kagawa, T. Takasawa, B. Zhang, M-W. Seo, K. Imai, J. Yamamoto, M. Kinjo, S. Terakawa, K. Yasutomi, and S. Kawahito, " 10×10 -pixel 606kS/s multi-point fluorescence correlation spectroscopy CMOS image sensor," SPIE Photonics West, Imaging, Manipulation, and Analysis of Biomolecules, Cells, and Tissues XII, vol. 8947, pp. 1-7, Feb. 2014.
 6. B. Zhang, K. Kagawa, M-W. Seo, K. Yasutomi, and S. Kawahito, "Multi-aperture System with Selective Averaging for RTS Noise and Dark Current Reduction," The 15th Takayanagi Kenjiro Memorial Symposium, S4-5, pp.1-5, Nov. 2013.

7. K. Kagawa, T. Takasawa, B. Zhang, M-W. Seo, K. Imai, J. Yamamoto, M. Kinjo, K. Yasutomi, S. Terakawa, and S. Kawahito, "A CMOS Image Sensor with High-speed Pixel-parallel Pipelined Readout Channels for Multi-point Fluorescence Correlation Spectroscopy," International Conference on Solid State Devices and Materials (SSDM), H-1-3, pp. 876-877, Sep. 2013.
8. K. Kagawa, B. Zhang, M-W. Seo, S. Kawahito, Y. Kominami, K. Yamada, S. Yoshida, and S. Tanaka, "Dual-Band Multi-Aperture Enhanced Redox Imaging of Colonic Adenomas for Endoscopes with a High-Performance CMOS Imager," 35th Annual International Conference of the IEEE EMBS, ThC06.1, pp.1414-1417, Jul. 2013.

National Symposia and Workshops

1. B. Zhang, K. Kagawa, T. Takasawa, M-W. Seo, K. Yasutom, S. Kawahito, "Multi-aperture imaging system with selective averaging for noise reduction," 第 16 回情報フォトニクスグループ研究会 (秋合宿) I-02, Sep. 2015.
2. 久下沼国之, 小室孝, 張博, 香川景一郎, 川人祥二, "低照度マルチアパーチャ画像からのデプスマップ推定," 映像情報メディア学会情報センシング研究会 (IST), 映像情報メディア学会技術報告 vol.39, no.17, pp.5-7, May 2015.
3. B. Zhang, K. Kagawa, T. Takasawa, M-W. Seo, K. Yasutom, S. Kawahito, "A high-sensitivity 2X2 multi-aperture color camera based on selective averaging," 映像情報メディア学会情報センシング研究会 (IST), 映像情報メディア学会技術報告, vol.39, no.16, pp.25-28, Mar. 2015.
4. 望月風太, 香川景一郎, 沖原伸一郎, 徐珉雄, 張博, 高澤大志, 安富啓太, 川人祥二, "画素内圧縮型マルチアパーチャ超高速イメージセンサによる 200Mfps バースト撮影," 映像情報メディア学会情報センシ

- ング研究会 (IST), 映像情報メディア学会技術報告, vol.39, no.16, pp.45-48, Mar. 2015.
5. 張博, 香川景一郎, 澤大志, 徐珉雄, 安富啓太, 川人祥二, “選択的平均に基づく高感度 2 × 2 マルチアパーチャカラーカメラ,” 第3回静岡大学技術展, Mar. 2015.
 6. P-S. Sivakumar, K. Kagawa, M-W. Seo, B. Zhang, T. Takasawa, K. Yasutomi, S. Kawahito, “Dark current and random noise measurement of 10x10-pixel multi-point fluorescence correlation spectroscopy CMOS image sensor,” IST, 2nd Asian Image Sensors and Imaging Systems Symposium, vol.38, no.47, IST2014-68, Dec. 2014.
 7. H. Suzuki, K. Kagawa, B. Zhang, M-W. Seo, T. Takasawa, K. Yasutomi, S. Kawahito, “A 4T-PWM CMOS image sensor for low power,” IST 2nd Asian Image Sensors and Imaging Systems Symposium, vol.38, no.47, IST2014-79, pp.53-54, Dec. 2014.
 8. 香川景一郎, P-S. Sivakumar, 高澤大志, 張博, 徐珉雄, 山本条太郎, 金城政孝, 安富啓太, 川人祥二, “多点蛍光相関分光 CMOS イメージセンサの特性評価,” Optics and Photonics Japan 2014, 5D1, Nov. 2014.
 9. 香川景一郎, 鈴木裕貴, 張博, 徐珉雄, 高澤大志, 安富啓太, 川人祥二, “4T-PWM イメージセンサの低電圧・低消費電力化の検討,” 映像情報メディア学会情報センシング研究会 (IST), 映像情報メディア学会技術報告, vol.38, no.37, pp. 5-8, Sep. 2014.
 10. 張博, 香川景一郎, 徐珉雄, 安富啓太, 川人祥二, “A high-sensitivity multi-aperture camera based on selective averaging,” COI「精神的価値が成長する感性イノベーション拠点」2014 夏の研究会, 光創起 002, pp.18, Sep. 2014.
 11. 香川景一郎, 徐珉雄, 山本条太郎, 西岡優起, 高澤大志, 張博, P-S. Sivakumar, 安富啓太, 金城政孝, 川人祥二, “多点多機能共焦点顕

- 微鏡に向けた CMOS イメージセンサの開発,” 2014 年第 39 回工学シンポジウム, 『工学システム・光学素子の設計,製作,評価を中心として』 講演予稿集, pp.5-6, Jun. 2014.
12. 鈴木裕貴, 香川景一郎, 張博, 安富啓太, 川人祥二, “埋込フォトダイオードを用いた PWM 画素読み出し方式 CMOS イメージセンサの検討,” 映像情報メディア学会情報センシング研究会 (IST), 映像情報メディア学会技術報告, vol. 38, no.20, pp. 5-7, Jun. 2014.
13. 鈴木裕貴, 香川景一郎, 張博, 安富啓太, 川人祥二, “PWM 画素読み出し方式を用いた低暗電流・低消費電力 CMOS イメージセンサの検討,” LSI とシステムのワークショップ 2014, 学生部門-2, PS-2-1~PS-2-8, May 2014
14. B. Zhang, K. kagawa, T. Takasawa, M-W. Seo, K. Yasutomi, S. Kawahito, “Low Noise Multi-aperture Camera by Selective Averaging,” 映像情報メディア学会, 情報センシング研究会 (IST), vol.38, no.15, pp. 31-34, Mar. 2014.
15. 張博, 香川 景一郎, 徐珉雄, 安富啓太, 川人祥二, “Multi-aperture system with selective averaging for RTS noise and dark current reduction,” 電気学会東海支部連合大会, 講演論文集, G5-1, Sep. 2013.
16. 張博, 香川景一郎, 徐珉雄, 安富啓太, 川人祥二, “低ノイズ・高ダイナミックレンジ CMOS イメージセンサに基づくマルチアパーチャカメラ,” 日本光学会 第 7 回新画像システム・情報フォトニクス研究討論会, 講演予稿集 B-6, pp. 48-49, Jun. 2013.

Acknowledgements

First of all, I would like to express my deep gratitude to Prof. Dr. Keiichiro Kagawa for giving me opportunity to be under his supervision. His wealth of knowledge and perceptiveness helped me avoiding detours in study.

I sincerely thank associate Prof. Dr. Shoji Kawahito for guiding me work on the exciting topic, for serious and patient guidance on my study, and for instructive advice and useful suggestions on my thesis.

Secondly, I would like to thank and deep appreciation to Prof. Dr. Shoji Kawahito, Prof. Dr. Hideki Asai and Prof. Dr. Gosuke Ohashi for valuable comments and suggestions regarding this thesis.

I would like to thank Dr. Min Woong Seo for teaching me in low-noise pixel design. I would like to thank all the members of HSC for development of the high performance image sensor. Certainly, I would like to thank assistant Prof. Dr. Keita Yasutomi and Dr. Zhuo Li for their kindly help to dispose of problems in study. Also I would like to thank Dr. Mars Kamel, Mr. Taishi Takasawa, Mr. Michio Fukuda, Ms. Rumi Fujihara, Ms. Satoko Tsuchiya, Ms. Seiko Nakamura, and all the members of Imaging Devices Laboratory for continuous help and support and making the Lab. a big warm family, let me feeling comfortable and enjoyable here.

Finally and definitely not the least, I would like to thank my families. For giving me unlimited support to follow my own will. I deeply regret for being unable to take care of my grandmother and my parents. I would like to thank my wife for always being there for me. It is her who make this strange place a home where I can always turn for comfort, support, and encouragement. Also, I want to thank my son for bringing endless laughter and happiness.